Åbo Akademi University

Harri Aarnio

Photoexcitation dynamics in organic solar cell donor/acceptor systems

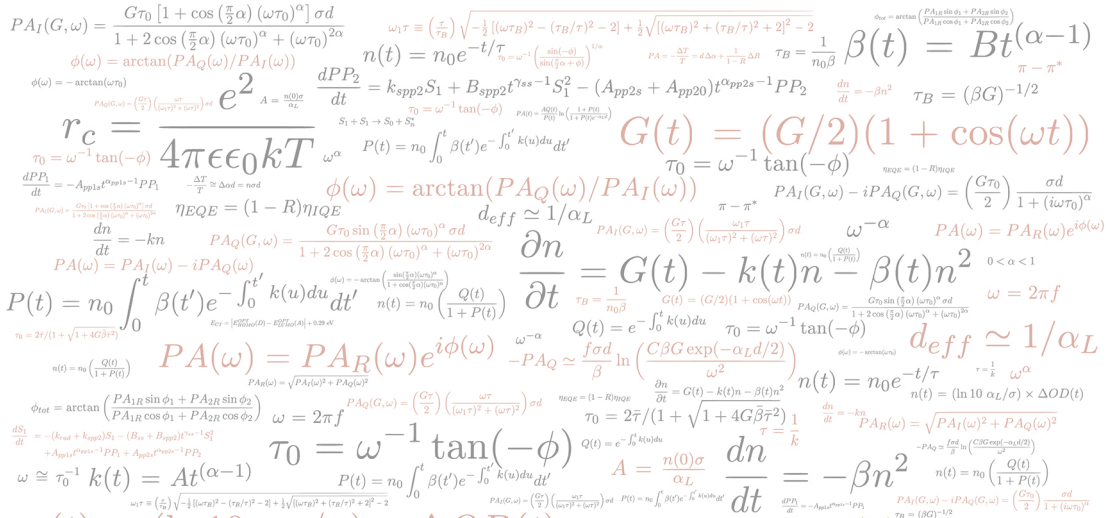

Photoexcitation dynamics in organic solar cell donor/acceptor systems

Harri Aarnio

Physics
Center for Functional Materials
Department of Natural Sciences
Åbo Akademi University
Åbo, Finland, 2012

Supervisor

Professor Ronald Österbacka
Åbo Akademi University

Pre-examiners

Professor Helge Lemmetyinen
Tampere University of Technology

Associate Professor Stefan Meskers
Eindhoven University of Technology

Opponent for the public defense

Professor John de Mello
Imperial College London

ISBN 978-952-12-2803-2
Painosalama Oy – Åbo 2012

Contents

Preface

This thesis is based on my research in the Organic Electronics group at the Department of Natural Sciences / Physics at Åbo Akademi University and within the Center for Functional Materials. The work has been carried out under the supervision of Prof. Ronald Österbacka during the years 2004 – 2012. After finishing my Master's thesis on recombination in polymeric solar cell materials in spring 2004, I was asked by Ronald and Prof. Emer. Henrik Stubb to continue doing research under the same topic. I am very grateful to them for this opportunity and for introducing me to the interesting field of organic electronics. The work has been fun, challenging and has felt purposeful. I have appreciated the interdisciplinary nature of this field and the time spent both in the lab and in the office. During most of my time as a PhD student I have also worked as a teaching assistant. This has significantly slowed down my research, but the assistant duties have been a rewarding and educating experience. I would like to thank both Ronald and Prof. Markus Lindberg, as well as docents Johan Lindén and Tom Lönnroth for this opportunity.

I would like to express my deepest gratitude to Ronald for all his help during the years and his patience with the slow progress. Also, Ronald's ability to arrange for funding via various projects and other channels has been a blessing, thank you! I would also like to thank Svenska Tekniska Vetenskapsakademien i Finland for a personal scholarship, which enabled me to do full-time research for a year.

I have had the pleasure to work with many people during my time at Åbo Akademi, as well as during several visits to Linköping and Lund

Universities. I would especially like to mention Dr. Markus Westerling, who introduced me to the measurement setups in our optical laboratory and explained the theoretical aspects of my coming work in a very detailed and educating manner. I am very grateful to Dr. Kjell-Mikael Källman for the invaluable technical assistance in our own labs, to Dr. Fengling Zhang in Linköping for teaching me the basics of making and measuring organic solar cells, and to Dr. Arkady Yartsev in Lund for assisting with the complicated setup used for ultrafast photoinduced absorption measurements. I would also like to thank our secretary Maisa Mantere for all the help with practical details. A big thank you goes to all my colleagues and friends at Physics for an inspiring and relaxed working environment! It has been great working with you and getting to know you. Furthermore, finalizing the layout of this thesis has been easy thanks to LaTeX code kindly provided by Dr. Fredrik Jansson, thank you for that. I am also grateful to my friend Jenna Hastelow for valuable feedback on the language in this thesis.

My family means more to me than I can describe. I am deeply grateful to my parents Gunilla and Veikko, my brothers Marko and Jukka and my sister Johanna for being there and supporting me, no matter what. Finally, I would like to thank my wife Jetta for her love, patience, support, and encouragement during my long days and seemingly never-ending writing, and also my daughter Lumi, whose endeavors are more fascinating and delightful than anything presented in this thesis! You always bring a smile on my face!

Harri Aarnio
Åbo, September 2012

List of publications

This thesis is based on the five original publications listed below. The publications are included at the end of the thesis with the permission of the publishers.

I. *Recombination studies in a polyfluorene copolymer for photovoltaic applications*,
H. Aarnio, M. Westerling, R. Österbacka, M. Svensson, M.R. Andersson, T. Pascher, J. Pan, V. Sundström and H. Stubb,
Synthetic Metals **155**, 299 (2005).

II. *Photoinduced absorption in an alternating polyfluorene copolymer for photovoltaic applications*,
H. Aarnio, M. Westerling, R. Österbacka, M. Svensson, M.R. Andersson, and H. Stubb,
Chemical Physics **321**, 127 (2006).

III. *Photoexcitation dynamics in an alternating polyfluorene copolymer*,
M. Westerling, H. Aarnio, R. Österbacka, H. Stubb, S.M. King, A.P. Monkman, M.R. Andersson, K. Jespersen, T. Kesti, A. Yartsev and V. Sundström,
Physical Review B **75**, 224306 (2007).

IV. *Spontaneous charge transfer and dipole formation at the interface between P3HT and PCBM*,
H. Aarnio, P. Sehati, S. Braun, M. Nyman, M.P. de Jong, M. Fahlman and R. Österbacka,
Advanced Energy Materials **1**, 792 (2011).

V. *Bimolecular recombination in regioregular and regiorandom poly(3-hexylthiophene):PCBM using photoinduced absorption spectroscopy*,
H. Aarnio and R. Österbacka,
Energy Procedia, Submitted (2011).

Author's contribution

The theoretical foundation for this work lies mainly on the previous work by Dr. Markus Westerling. The contribution of the author to the publications included in this thesis is the following:

I. The author did all of the experimental work together with M. Westerling, T. Pascher and J. Pan, wrote the first draft of the manuscript and finalized it together with the co-authors.

II. The author did all of the experimental work together with M. Westerling, part of the theoretical work regarding the phase information, wrote the first draft of the manuscript and finalized it together with the co-authors.

III. The author did all of the experimental work together with M. Westerling, S. M. King, K. Jespersen, T. Kesti and A. Yartsev, participated in close collaboration with M. Westerling in the modeling of the data and in writing the manuscript.

IV. The author did all the experimental work except for that related to the UV photoelectron spectroscopy measurements, analyzed the results together with the co-authors, wrote the first draft of the manuscript and finalized it together with the co-authors.

V. The author did all the experimental work, analyzed the results, wrote the manuscript and finalized it together with the co-author.

Chapter 1

Introduction

1.1 Background

The discovery of conducting and semiconducting polymers by A. J. Heeger, A. MacDiarmid and H. Shirakawa in 1977 introduced a new field of technology, namely organic electronics [1]. Research in this field has been very active during the last years, with advances in both materials development and device design. The most prominent subfield of organic electronics is organic light-emitting diodes (OLEDs), with OLED displays already used in consumer electronics. Organic solar cells are also drawing widespread attention in the scientific community. Increased awareness of environmental issues such as global warming and pollution, as well as distrust in nuclear energy as a safe and problem-free energy source, has lead to a grown interest in alternative energy sources to satisfy the ever increasing demand for energy. For many applications, such as lighting and low-power home appliances, solar energy is an interesting and viable option. In off-grid locations solar energy is already commonly used. The main downside with solar cells based on conventional silicon designs is a relatively high panel price and, therefore, it is of great interest to develop solar cell technology that is both easy and cheap to manufacture, as well as environmentally sustainable.

Organic solar cell research is focused on three main device types, i.e. dye-sensitized solar cells (or Grätzel cells) [2], bulk-heterojunction solar

cells [3], and small-molecule solar cells [4]. The Grätzel cells are currently ahead when it comes to efficiency with 12.3 % power conversion efficiency [5], followed by small-molecule cells with 10.7 % [6], and bulk heterojunction cells with 10.6 % [7]. The main disadvantage with Grätzel cells is their electrochemical operating principle, which requires an electrolyte, carefully capped between two sheets of glass or plastic to prevent leakage and evaporation. Small-molecule solar cells are typically made by co-evaporation of small organic compounds in a controlled manner, which requires specialized equipment. Advantages of the bulk heterojunction solar cells include a solid state design and better compatibility with roll-to-roll manufacturing techniques. On the downside, the typical bulk heterojunction solar cells consist of disordered materials in a complex morphology, which complicates the photophysical processes in them [8]. Furthermore, the polymers used are often sensitive to impurities, moisture and oxygen [9, 10]. Developing new materials, sealing methods and ways for controlling the morphology of the bulk heterojunction are therefore crucial issues, and understanding the physical processes in the bulk heterojunction materials is an important prerequisite for this.

1.2 The aim of the work

This work is focused on two solar cell polymers, APFO3 and P3HT, which are described in detail in Section 3.1. APFO3 is a promising polymer that is particularly interesting because of its internal donor-acceptor character. One of the goals in this work is identifying and characterizing the different photoexcitations and their dynamics in the pure APFO3 polymer and in the blends of APFO3 with an electron acceptor.

P3HT is the best known model polymer for organic solar cells, and P3HT based cells are well known to show a strongly reduced recombination of charges, ordering of the polymer chains and power conversion efficiencies of up to 5% [11,12]. Due to significant recombination of charges, the power conversion efficiencies for APFO3 based solar cells do not quite reach those for P3HT based cells [13]. Another goal in this work is thus to gain a

better understanding of the charge generation and recombination processes which make P3HT a better-performing solar cell material than APFO3. In particular, the effect of polymer chain ordering on the photophysics is explored, as well as the influence of interfacial dipoles on the recombination of charges.

1.3 Donor/acceptor systems

A solar cell with the active layer consisting of a single organic material does not function well [14]. The efficiency for spontaneous charge separation in such a layer is typically on the order of $10^{-3} - 10^{-2}$% [3, 15]. As there is no driving force to separate electrons and holes, the internal power conversion efficiency is severely limited by recombination. The key for higher internal power conversion efficiency is to combine an electron donating and an electron accepting material together to provide a strong local driving force for charge separation. For an initially generated singlet exciton to be efficiently separated into an electron and a hole, the exciton needs to be close to a donor/acceptor interface. Typical singlet exciton diffusion distances are in the range of $\sim$ 10 nm [16], and excitons within that distance from a donor/acceptor interface are likely to be separated with close to 100 % efficiency [17]. This presents a problem, as the absorption coefficient of polymers, even at optimal wavelengths, is not high enough to allow for complete absorption of the sunlight in a 10 nm layer. Efficiency loss in bilayer devices will therefore arise from either recombination of excitons far from the donor/acceptor interface (thick absorbing layer) or transmission of incident light through the device (thin absorbing layer). To circumvent this problem, the bulk heterojunction concept was introduced [3]. Here, the electron donating and accepting materials are mixed together, forming a three dimensional network of interfaces in the bulk of the blend. With phase separated region sizes similar to the exciton diffusion distance, photon absorption events throughout the blend are likely to result in separated electrons and holes [18, 19]. These can then travel via separate pathways to their respective contacts, minimizing recombination.

The materials discussed in this work fall into three categories, electron donors, electron acceptors and materials with an internal donor-acceptor character. The electron donating or accepting character of a molecule in relation to another is determined by the electron affinities of the molecules. The molecule with the higher electron affinity is called an electron acceptor, and the molecule with an lower electron affinity is called an electron donor. Electron affinity is defined as the energy difference between the vacuum energy and the lowest unoccupied molecular orbital (LUMO) of a neutral molecule.

In bulk heterojunction solar cells, the donor material is mainly responsible for photon absorption. When the generated exciton diffuses to an interface with an acceptor material, the electron will transfer from the LUMO of the donor to the lower-energy LUMO of the acceptor. Holes, which can be viewed as an absence of an electron in the highest occupied molecular orbital (HOMO), effectively having a positive charge, tend to move upward in energy and prefer to stay on the donor. Sandwiching the active layer between two electrodes with different work functions provides a driving force that will cause the electrons and holes to travel towards respective contacts. The charge separation and transport in a device is schematically presented in Figure 1.1.

1.4 Solar cell efficiency

The main coefficients used to describe solar cell device efficiencies are the power conversion efficiency, which measures how much of the power of the incident light is converted to electrical power, the fill factor, which measures how much of the theoretical maximum power of the cell is actually obtained, and the external quantum efficiency (EQE), which measures the fraction of incoming photons of a given wavelength converted to extracted electrons.

The external quantum efficiency (η_{EQE}) of a solar cell is given by

$$\eta_{EQE} = (1 - R)\eta_{IQE}, \tag{1.1}$$

where R is reflection loss and (η_{IQE}) is the internal quantum efficiency, i.e.

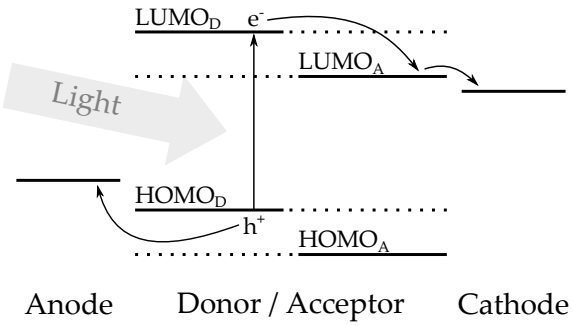

Figure 1.1: Schematic diagram showing the charge generation process in an organic solar cell. The dotted energy levels indicate that the donor and acceptor are mixed together, forming an interpenetrating network.

the efficiency for an absorbed photon giving rise to a charge pair collected at the electrodes. There are basically four processes involved in determining η_{IQE}, namely the photon absorption efficiency η_A, the exciton diffusion efficiency η_{ED}, the charge transfer efficiency η_{CT}, which is the main focus in this work, and finally the charge collection efficiency η_{CC} [20]:

$$\eta_{IQE} = \eta_A \eta_{ED} \eta_{CT} \eta_{CC}. \tag{1.2}$$

There are several criteria a semiconducting organic polymer needs to meet to be a good component in the active layer of an organic solar cell. For example, the polymer working as a donor needs to absorb as much of the sunlight as possible, meaning that there should be maximum overlap between the absorption spectrum of the polymer and the spectrum of the sunlight. Since the intensity of the sun peaks in the infrared wavelengths, it is important that polymers for solar cell applications are tailored to have an extended absorption in the infrared. The absorption is determined by the optical gap of the polymer, i.e. the difference in energy between the HOMO and LUMO levels. For maximum η_A the absorption coefficient, which varies with wavelength, should be as high as possible. These are

typically not limiting factors with current polymers, which can have optical gaps of < 2 eV and absorption coefficients larger than 10^5 cm^{-1}.

The morphology of the donor/acceptor blend needs to be such that the initially generated excitons can reach an interface before they recombine. This is the requirement for a high η_{ED}. The regions in the bulk heterojunction should optimally be smaller than the exciton diffusion distance in the given materials. The morphology of the bulk heterojunction can be tuned by using different solvents, changing the drying time and conditions, and by applying heat treatments (also called annealing) to the dried films [21–24].

After reaching the donor acceptor interface, it is important that as many of the optically generated singlet excitons as possible dissociate into free electrons and holes, giving a η_{CT} close to 1. Losses here mainly originate from the inability of separated charges to overcome their mutual Coulomb potential and escaping the interface, resulting in either geminate recombination or formation of other types of excited states. Several types of excitons and charges can exist in a solar cell material at various stages, the central ones for this work will be described briefly in the next section.

Recombination is also a limiting factor during charge collection, when separated charges travel to the electrodes to be extracted. Low recombination, and thus a high η_{CC}, is closely linked to the morphology of the polymer film, and also the intrinsic chain mobility [25, 26]. High order typically enhances mobility, while charge trapping due to various defects reduces it. Low mobility causes buildup of charges in the active layer and thus increases recombination. Suitable electrodes are also important for efficient charge extraction [27].

1.5 Photophysics of conjugated polymers

Conjugated polymers can host a number of different neutral and charged excitations, out of which the central ones for this work will be briefly presented here. When a photon with an energy higher than the optical gap of the polymer (E_{gap}) is absorbed, an electron will be promoted to the first excited state, i.e. from the HOMO to the LUMO, creating a singlet exci-

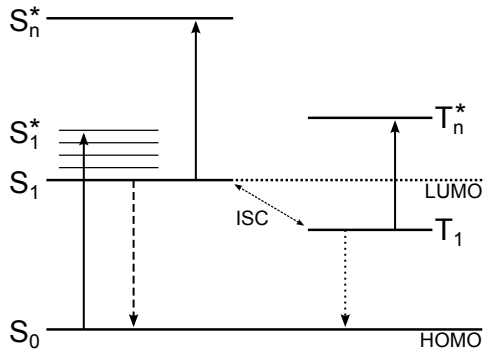

Figure 1.2: Schematic view of singlet and triplet excitons. Solid arrows represent allowed excitation events (optical or via EEA), the dashed arrow a spin-allowed recombination channel and the dotted arrow a spin-forbidden recombination channel. Intersystem crossing is indicated separately.

ton (S). The singlet exciton is an electrically neutral elementary excitation, consisting of a Coulombically bound electron-hole pair with opposing spins for the electron and the hole. This allows for rapid recombination back to the ground state S_0, and consequently the singlet exciton lifetime is short, typically on the order of pico- to nanoseconds. Immediately after the photoexcitation event, the singlet exciton is in the first excited state (S_1^*), with some excess energy compared to the thermalized S_1 state. The singlet exciton (S) is typically of Frenkel type, delocalized over three to four repeat units of the polymer chain [28]. In some cases, when allowed by spin-orbit coupling, the electron can flip its spin via intersystem crossing (ISC), and form a triplet exciton (T) [29]. In the triplet state the recombination back to the ground state is spin-forbidden, and consequently the triplet exciton lifetime is long. The singlet and triplet exciton energy levels are illustrated in Figure 1.2

At high concentrations of singlet excitations so called exciton-exciton annihilation (EEA) can take place according to $S_1 + S_1 \rightarrow S_0 + S_n^*$, acting as a bimolecular recombination pathway [30–32]. The highly excited S_n^*

state has a high probability for dissociation and provides a route for charge separation. The singlet exciton can also dissociate by electron (or hole) transfer to a neighboring conjugated segment or a neighboring chain or molecule.

If an electron and hole can separate a larger distance than the Coulomb radius, two free charges, a positive and a negative polaron (P^+ and P^-) are formed. The polarons involve a structural relaxation of the polymer, confining the charge in a potential well [33]. This gives rise to new states within the optical gap of the polymer. These states have two characteristic dipole allowed transitions, P_1 and P_2. In ordered regions of the polymer, delocalization of the polaron over neighboring chains splits the energy levels and forms a delocalized polaron (DP) [34, 35]. The delocalized polaron has the characteristic transitions DP_1 and DP_2, analogous to P1 and P2 for the polaron, but blue- and redshifted respectively, due to less structural relaxation. Schematic energy levels and transitions for polarons and polaron pairs, as well as for delocalized polarons, are presented in Figure 1.3 [34, 36]. Polaron pairs (PP) are electron and hole polarons that remain Coulombically bound. The electron and hole can be located on the same chain or on neighboring chains or molecules, forming an intra- or interchain polaron pair (PP_{intra} or PP_{inter}), respectively [37–39]. The polaron pair stays formed as long as the electron-hole separation is smaller than the the Coulomb radius r_c. The Coulomb radius is given by

$$r_c = \frac{e^2}{4\pi\epsilon\epsilon_0 kT}, \tag{1.3}$$

where e is the electron charge, ϵ and ϵ_0 the relative and vacuum permittivities, respectively, k the Boltzmann constant and T the temperature.

When closely mixing an electron donor and an electron acceptor, the photophysics of the blend change compared to the neat polymer. The main difference is a rapid ($\sim$ 45 fs) charge transfer from the donor to the acceptor [40]. This essentially quenches the presence of singlet excitations in the blend, and consequently also the generation of triplet excitations via intersystem crossing. For the same reason, generation of polaron pairs, polarons and delocalized polarons is very efficient in these systems, which

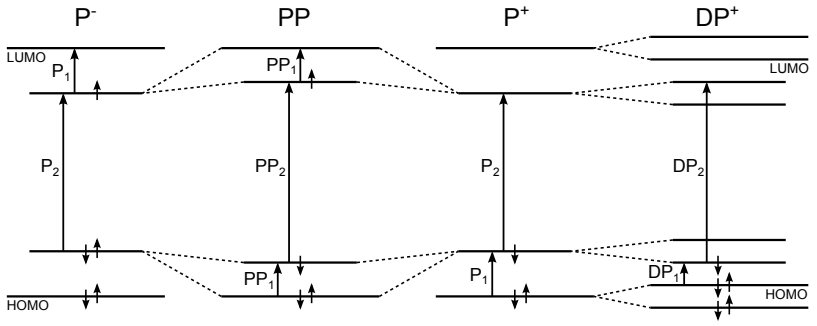

Figure 1.3: Schematic energy levels of the charged excitations and their strongest dipole allowed transitions [34, 36].

is why they have been successful in solar cell applications.

Due to the close proximity of the donor and acceptor molecules, wave function overlap introduces new so called charge transfer (CT) states at the donor/acceptor interfaces (Figure 1.4) [41–48]. Experimental evidence shows that these new states have a weak absorption lower in energy than either the donor or acceptor molecules alone [41, 42]. The CT state can be optically excited using sub-bandgap light, and the charges populating the CT state can be separated into free charges, as discussed in Paper IV in this work, as well as in references [45, 46, 49, 50]. The CT state also plays a role as an intermediate step during recombination, as evidenced by electroluminescence (EL) and photoluminescence (PL) measurements, where the wavelength of the emitted light corresponds to the energy of the CT state, E_{CT} [48, 49, 51, 52]. Predicting E_{CT} is possible by using the experimentally determined relation

$$E_{CT} = \left| E^{OPT}_{HOMO}(D) - E^{OPT}_{LUMO}(A) \right| + 0.29 \text{ eV} \tag{1.4}$$

by Veldman et al., where $E^{OPT}_{HOMO}(D)$ and $E^{OPT}_{LUMO}(A)$ are the optically detected HOMO and LUMO levels for the donor and acceptor, respectively [53]. The energy of the CT state is also related to the open circuit voltage

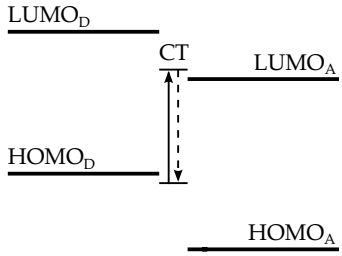

Figure 1.4: Schematic view of a charge transfer state (labeled CT) at the donor/acceptor interface.

V_{OC} via the approximate relation $E_{CT} = eV_{OC} - 0.5$ eV [46, 53]. In a different approach, the CT state can be viewed as an excited state of a large molecular complex, for which E_{CT} can be calculated by quantum chemical methods [54, 55]. In general, the CT states have been found to play an important role in the photophysics of donor/acceptor blends, but the exact nature and role of this state are still under investigation.

1.5.1 Recombination

In a first order or monomolecular recombination process the recombination rate depends linearly on the excitation concentration n and is given by $dn/dt = -kn$, where k is the monomolecular rate constant. In a second order or bimolecular recombination process the recombination rate depends on n^2, and is given by $dn/dt = -\beta n^2$, where β is the bimolecular rate constant. These rate equations, together with the solutions and the corresponding lifetimes are presented in Table 1.1. While the monomolecular lifetime τ is uniquely defined, the bimolecular lifetime τ_B depends on the initial excitation concentration n_0.

When an electron and hole originating from the same photon recombine, the process is called geminate. When electrons and holes of different origin recombine, the process is called non-geminate. Monomolecular recombination is typically a geminate process, whereas bimolecular recombination is

Table 1.1: Rate equations for first and second order recombination processes, the solutions for the time dependent excitation concentrations $n(t)$, and the corresponding excitation lifetimes.

Order	Equation	Solution	Lifetime
1^{st}	$\frac{dn}{dt} = -kn$	$n(t) = n_0 e^{-t/\tau}$	$\tau = \frac{1}{k}$
2^{nd}	$\frac{dn}{dt} = -\beta n^2$	$n(t) = \frac{n_0}{1 + \frac{t}{\tau_B}}$	$\tau_B = \frac{1}{n_0 \beta}$

non-geminate.

The states in disordered organic semiconductors generally follow a Gaussian distribution in energy. Experimental evidence and simulations suggest, however, that the distribution of states (DOS) is not a perfect Gaussian, but has an exponential tail of trap states as illustrated in Figure 1.5 [56–58]. Transport in this kind of a system can be described using Marcus theory [59]. Charges and triplets can move to neighboring sites by hopping (tunneling), and the probability to do so depends on the energy and distance of the neighboring localized states. This has consequences for the recombination dynamics. As charges undergo random walk by hopping in a DOS, they thermalize over time (Figure 1.5 b)). This effectively leads to time dependent rate coefficients $k(t)$ and $\beta(t)$, which can alternatively be seen as a distribution of lifetimes for the excitations, giving rise to dispersive recombination dynamics [60–62].

The exact time-dependence of the rate coefficients depends on the shape of the DOS, and especially on the tail of the distribution. The Gaussian DOS with an exponential tail of trap states leads to decays with power law character [56–58, 63]. The coefficients $k(t)$ and $\beta(t)$ can thus be approximated in a limited time interval with the power laws $k(t) = At^{(\alpha-1)}$ and $\beta(t) = Bt^{(\alpha-1)}$, where A and B are characteristic recombination parameters, and α is a dispersion parameter taking values between 0 and

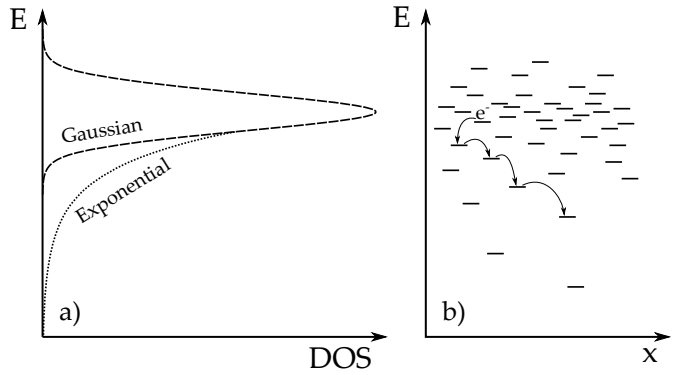

Figure 1.5: a) Gaussian density of states (dashed) with an exponential tail (dotted). b) Thermalization of an electron in a distribution of states corresponding to a) in one spatial coordinate.

1 [62, 64, 65]. In the $\alpha \to 1$ limit, the time-independent (nondispersive) rates are obtained.

A general rate equation of Riccati type, including both mono- and bimolecular recombination as well as a generation rate $G(t)$, can be written as

$$\frac{\partial n}{\partial t} = G(t) - k(t)n - \beta(t)n^2. \tag{1.5}$$

To find the solution for equation (1.5) in the time domain, an initial condition $n(t = 0) = n_0$ is assumed instead of the generation $G(t)$. This leaves a differential equation of Bernoulli type to be solved, yielding [62]:

$$n(t) = n_0 \left(\frac{Q(t)}{1 + P(t)} \right), \tag{1.6}$$

where

$$Q(t) = e^{-\int_0^t k(u)du} \tag{1.7}$$

and

$$P(t) = n_0 \int_0^t \beta(t') e^{-\int_0^{t'} k(u)du} dt'. \tag{1.8}$$

This solution can account for all time dependences for $k(t)$ and $\beta(t)$, and a combination of monomolecular and bimolecular recombination. Assuming nondispersive recombination and either pure monomolecular or pure bimolecular recombination, the solution simplifies to those presented in Table 1.1. Solutions to equation (1.5) in the frequency domain will be described in Chapter 2.

Chapter 2

Photoinduced absorption

Photoinduced absorption (PA) spectroscopy is a pump-probe technique, which involves an excitation (pump) beam that generates photoexcitations in a sample and a probe beam that monitors the resulting change in transmission through the sample. The measured quantity is typically the normalized change in transmission, $\Delta T/T$. The PA arises in part from a change $\Delta\alpha$ in the linear absorption coefficient α, and in part from a change ΔR in the reflection coefficient R of the film. Assuming a film of thickness d and reflection only off the front surface of the film, we can write [66]:

$$PA = -\frac{\Delta T}{T} = d\,\Delta\alpha + \frac{1}{1-R}\,\Delta R. \tag{2.1}$$

The first term in the above equation is typically more than an order of magnitude larger than the second term, and thus contribution from the change in the reflection coefficient is typically neglected in PA [66–68]. For a thin film where the pump light is absorbed uniformly through the thickness d of the film, $\Delta\alpha$ is given by $\Delta\alpha = n\sigma$, where n is the concentration of generated excitations and σ the absorption cross-section of the excitations. We can now write

$$-\frac{\Delta T}{T} \cong \Delta\alpha d = n\sigma d. \tag{2.2}$$

In general, the excitation concentration n through a film follows Lambert-Beer's law $n(x) = \exp(-\alpha_L x)$, where α_L is the absorption coefficient at the

pump wavelength. For a thick film ($\alpha_L d \gg 1$), most of the light is absorbed in a thin layer close to the surface. To use equation (2.2) for a thick film, the film thickness d can be replaced by the approximate effective optical thickness $d_{eff} \simeq 1/\alpha_L$.

Sometimes the PA is expressed as a change in optical density, ΔOD. The relation between ΔOD and $-\Delta T/T$ is given by $-\Delta T/T = \Delta OD \ln 10$.

2.1 Continuous wave photoinduced absorption

Continuous wave PA (cwPA) measures the absorption of photogenerated excitations by modulating a continuous excitation light and detecting the changes in the transmitted probe light using a lock-in amplifier. If the lifetime of the photoexcitations is short compared to the period of the modulation, the resulting concentration of excitations n will be in phase with the modulation. If the lifetime is longer, there will be a significant amount of excitations in the probed film even when the pump is off, giving rise to an absorption that is phase-shifted compared to the modulation. The lock-in amplifier is a phase-sensitive instrument, and represents the phase-shifted signal in complex form where the real and imaginary parts are the in-phase (denoted by subindex I) and quadrature or out-of-phase (subindex Q) ΔT signals having 0 and $-\pi/2$ phase shifts relative to the pump, respectively:

$$PA(\omega) = PA_I(\omega) - iPA_Q(\omega). \tag{2.3}$$

The signal can also be represented in polar coordinates using the radius (subindex R) and the phase (ϕ) as

$$PA(\omega) = PA_R(\omega)e^{i\phi(\omega)}, \tag{2.4}$$

where

$$PA_R(\omega) = \sqrt{PA_I(\omega)^2 + PA_Q(\omega)^2} \tag{2.5}$$

and

$$\phi(\omega) = \arctan(PA_Q(\omega)/PA_I(\omega)). \tag{2.6}$$

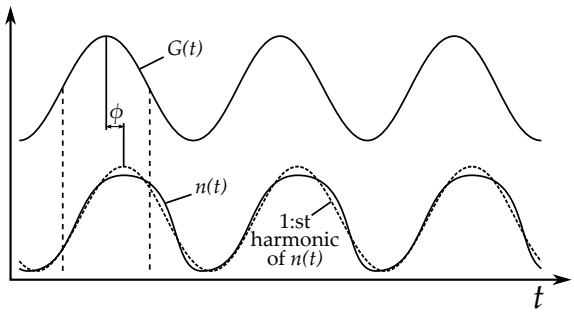

Figure 2.1: Schematic diagram of a sinusoidal generation $G(t)$, the resulting charge concentration $n(t)$ and the first harmonic of $n(t)$, which has a phase shift ϕ in relation to $G(t)$.

The arctan is here defined as the four quadrant arctan, which is defined to give phase values in all four quadrants ($-\pi \leq \phi \leq \pi$), as this is what the lock-in amplifier gives as well.

2.1.1 Sinusoidal generation

To solve equation (1.5) the generation G has to be defined. Westerling et al. have calculated an approximate solution assuming a sinusoidal generation $G(t) = (G/2)(1 + \cos(\omega t))$, where G is directly proportional to the excitation laser intensity I, $\omega = 2\pi f$ is the angular modulation frequency and f the modulation frequency in Hz [69, 70]. A general solution to equation (1.5) is known but complicated. By using harmonic analysis, only the first harmonic of the steady state periodic $n(t)$ signal is taken into account, as this is what the lock-in amplifier also measures. An illustration of the sinusoidal generation, the resulting $n(t)$ signal and its first harmonic approximation is shown in Figure 2.1. Assuming a thin film ($\alpha_L d < 1$), no dispersion and steady state conditions in equation (1.5), Westerling et al. thus obtain the approximate steady-state solutions for PA_I and PA_Q in the frequency domain for sinusoidal generation [69, 70]:

$$PA_I(G,\omega) = \left(\frac{G\tau}{2}\right)\left(\frac{\omega_1\tau}{(\omega_1\tau)^2+(\omega\tau)^2}\right)\sigma d \tag{2.7}$$

$$PA_Q(G,\omega) = \left(\frac{G\tau}{2}\right)\left(\frac{\omega\tau}{(\omega_1\tau)^2+(\omega\tau)^2}\right)\sigma d, \tag{2.8}$$

with

$$\omega_1\tau \equiv \left(\tfrac{\tau}{\tau_B}\right)\sqrt{-\tfrac{1}{2}\left[(\omega\tau_B)^2-(\tau_B/\tau)^2-2\right]+\tfrac{1}{2}\sqrt{\left[(\omega\tau_B)^2+(\tau_B/\tau)^2+2\right]^2-2.}}$$

Here the bimolecular lifetime τ_B is defined as $\tau_B = (\beta G)^{-1/2}$. Westerling et al. obtained varying PA dependencies on G, τ, β and ω when either mono- or bimolecular recombination dominates ($\tau/\tau_B \ll 1$ or $\tau/\tau_B \gg 1$, respectively) and assuming $\omega\tau_B \ll 1$ or $\omega\tau_B \gg 1$. These dependencies are presented in Table 2.1 for reference. The condition $\omega\tau_B \ll 1$ can be reached by making G large and/or ω small, and $\omega\tau_B \gg 1$ can conversely be reached by making G small and/or ω large.

One way to determine the lifetime of a photoexcitation is to measure the modulation-frequency dependence of the PA signal for the wavelength where the excitation absorbs. The results from the frequency-dependence measurement can be modeled using equations (2.7) and (2.8). Theoretical frequency dependence curves for monomolecular, bimolecular and combined mono- and bimolecular recombination are presented in Figure 2.2 a). The slopes and the general shapes of the curves depicted in Figure 2.2 a) are independent of the recombination type. The PA_I changes from a constant value to ω^{-2} dependence with increasing frequency, whereas PA_Q changes from ω^1 to ω^{-1} dependence. The knee of the inphase and the maximum of the quadrature component depend on the lifetime and are located at $\omega\tau_{eff} \cong 1$, where τ_{eff} is an approximate effective lifetime.

As mono- and bimolecular recombination have different dependence on G, the excitation intensity dependence of the PA can be used to determine the type of recombination by observing the slope of the PA curves. The experimental curves can also be modeled using equations (2.7) and (2.8) to find numerical values for the recombination parameters. Monomolecular

Table 2.1: PA dependencies on G, τ, β and ω for combinations of the limits $\omega\tau_B \gg 1$, $\omega\tau_B \ll 1$, $\tau/\tau_B \ll 1$ and $\tau/\tau_B \gg 1$ in the case of sinusoidal generation $G(t)$. The conditions in the two topmost rows are most likely to be observed in an experiment [70]. The emphasized dependencies for PA_Q can be used to experimentally determine β or G.

Condition	PA_I	PA_Q
$\omega\tau_B \gg 1$ & $\tau/\tau_B \ll 1$	$\sim G\tau/(1+(\omega\tau)^2)$	$\sim G\omega\tau^2/(1+(\omega\tau)^2)$
$\omega\tau_B \ll 1$ & $\tau/\tau_B \gg 1$	$\sim (G/\beta)^{1/2}$	$\sim \omega/\beta$
$\omega\tau_B \gg 1$ & $\tau/\tau_B \gg 1$	$\sim \beta^{1/2}G^{3/2}/\omega^2$	$\sim G/\omega$
$\omega\tau_B \ll 1$ & $\tau/\tau_B \ll 1$	$\sim G\tau$	$\sim G\omega\tau^2$

recombination leads to linear excitation intensity dependence for both PA_I and PA_Q. Bimolecular recombination is characterized by PA_I showing $G^{3/2}$ dependence at low excitation intensities and $G^{1/2}$ dependence at high excitation intensities. At the same time PA_Q goes from linear dependence to a constant value with increasing excitation intensity. The excitation intensity dependences for monomolecular, bimolecular, and combined mono- and bimolecular recombination are plotted in Figure 2.2 b). For combined mono- and bimolecular recombination, the monomolecular recombination dominates at low excitation intensity masking the $G^{3/2}$ superlinear bimolecular dependence, and bimolecular recombination dominates at high excitation intensities masking the monomolecular linear intensity dependence.

If we are only interested in the recombination coefficient β, it can be obtained by observing the saturation of $PA_Q \sim \omega/\beta$ at high excitation intensities, when $\omega\tau_B \ll 1$. This is an approximation, however, as the measured PA_Q does not saturate, but will keep increasing logarithmically, as discussed in section 2.1.2. Previously Wohlgenannt et al. have shown that the PA_Q signal can also be used to obtain G, as PA_Q becomes proportional to the generation and independent of recombination when measuring

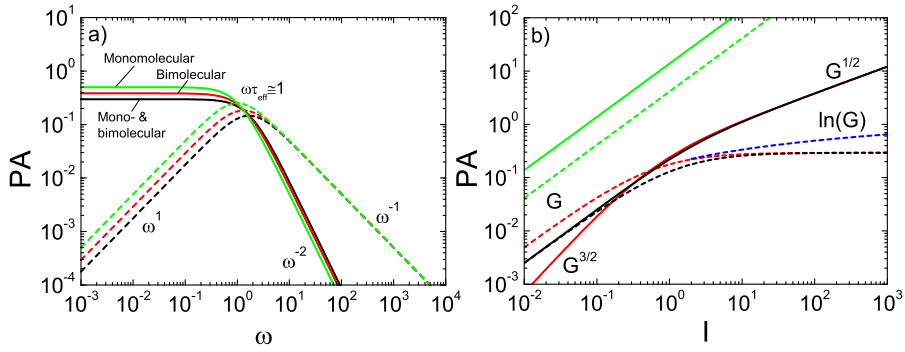

Figure 2.2: a) PA frequency dependence and b) PA intensity dependence for monomolecular (green), bimolecular (red) and combined mono- and bimolecular recombination (black). Both a) and b) are modeled after equations (2.7) and (2.8). In b), the high intensity part of the quadrature signal is also modeled using equation (2.9) (blue). Solid curves correspond to the inphase- and dashed curves to the quadrature components of the PA. The calculations have generally been done using $\tau = \beta = \sigma = d = 1$, as well as $G = 1$ in a) and $\omega = 1$ in b). The curve from equation (2.9) in b) was adjusted for illustrative purposes, and the monomolecular intensity dependence was shifted using $G = 100$ and $\tau = 0.3$ to avoid overlap.

far from steady state and when bimolecular recombination dominates [71].

2.1.2 Square wave generation

Assuming square wave generation (Figure 2.3), Westerling et al. also attempted to calculate the exact solution to equation (1.5) [62]. Due the complexity of $n(t)$, analytical solutions for PA_I and PA_Q similar to equations (2.7) and (2.8) are not given. The dependencies on G, τ, β and ω are essentially the same as those for the approximate solution presented in Table 2.1, with the exception for when $\omega\tau_B \ll 1$ and bimolecular recombination dominates ($\tau/\tau_B \gg 1$) [62, 72]. Then the PA_Q signal is shown to

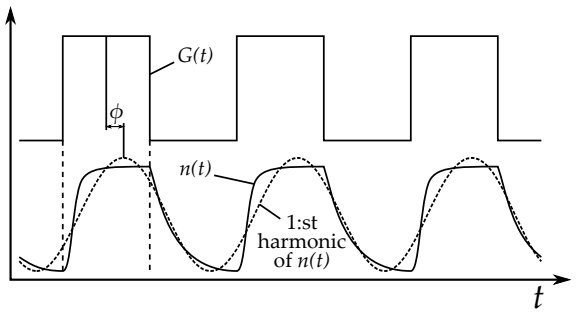

Figure 2.3: Schematic diagram of a square wave generation $G(t)$, the resulting charge concentration $n(t)$ and the first harmonic of $n(t)$, which has a phase shift ϕ in relation to $G(t)$.

have a logarithmic intensity dependence

$$-PA_Q \simeq \frac{f\sigma d}{\beta} \ln\left(\frac{C\beta G \exp(-\alpha_L d/2)}{\omega^2}\right), \tag{2.9}$$

where $C \simeq 1.46111$ [62]. Hence, instead of the saturation to $\sim \omega/\beta$ as presented in Table 2.1, we can use equation (2.9) to directly calculate β from the slope of the -PA$_Q$ signal plotted on a semi-logarithmic scale. The difference between the approximate solution for PA_Q and equation (2.9) is shown in Figure 2.2 b). In experiments, it is important to ensure that the modulation of the pump matches either a sinusoidal or square-wave shape as closely as possible, as the difference in the theoretical expressions stems directly from the shape of the modulation.

2.1.3 Dispersion

Dispersion in the cwPA experiments is typically accounted for by using an empirical Cole-Cole type function, as suggested by Epshtein et al. [60, 61]:

$$PA_I(G,\omega) - iPA_Q(G,\omega) = \left(\frac{G\tau_0}{2}\right)\frac{\sigma d}{1+(i\omega\tau_0)^{\alpha}}, \quad 0<\alpha<1. \tag{2.10}$$

Here, the PA response depends on a fractional power of the modulation frequency ω. The parameter τ_0 is an effective "mean" lifetime, and α is the dispersion coefficient. Different types of recombination can be catered for by defining τ_0 in a suitable way. For a monomolecular recombination process $\tau_0 = \bar{\tau}$, where $\bar{\tau}$ is the "mean" monomolecular lifetime, and for a bimolecular process $\tau_0 = (\bar{\beta}_0 G)^{-1/2}$, where $\bar{\beta}_0$ is the "mean" bimolecular rate coefficient [61, 62]. For a combined mono- and bimolecular process $\tau_0 = 2\bar{\tau}/(1+\sqrt{1+4G\bar{\beta}\bar{\tau}^2})$ [73]. The PA_I and PA_Q components can then be calculated [74]:

$$PA_I(G,\omega) = \frac{G\tau_0\left[1+\cos\left(\frac{\pi}{2}\alpha\right)(\omega\tau_0)^{\alpha}\right]\sigma d}{1+2\cos\left(\frac{\pi}{2}\alpha\right)(\omega\tau_0)^{\alpha}+(\omega\tau_0)^{2\alpha}} \tag{2.11}$$

$$PA_Q(G,\omega) = \frac{G\tau_0\sin\left(\frac{\pi}{2}\alpha\right)(\omega\tau_0)^{\alpha}\sigma d}{1+2\cos\left(\frac{\pi}{2}\alpha\right)(\omega\tau_0)^{\alpha}+(\omega\tau_0)^{2\alpha}}. \tag{2.12}$$

The dispersion will weaken the modulation frequency dependences of PA_I and PA_Q compared to the nondispersive case. The PA_I component will slowly turn from a constant value at low frequency to $\omega^{-\alpha}$ dependence for high frequency. PA_Q on the other hand, will turn from ω^{α} to $\omega^{-\alpha}$ dependence as the modulation frequency is increased [60]. This behavior is independent of the recombination type. PA_Q maintains a maximum at $\omega \cong \tau_0^{-1}$, where PA_I has reduced to half of its low frequency value. Observing the peak of the $PA_Q(\omega)$ signal thus provides a quick way to estimate the "mean" lifetime τ_0. Theoretical frequency dependence curves for combined mono- and bimolecular recombination with dispersion are presented in Figure 2.4 a).

Dispersive monomolecular recombination shows linear excitation intensity dependence both for PA_I and PA_Q [75]. If the recombination is dispersive and bimolecular, PA_I and PA_Q behave sublinearly for all G. At

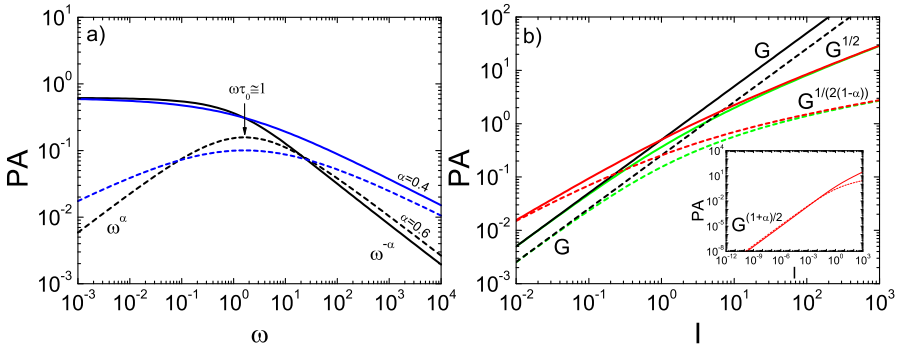

Figure 2.4: a) PA frequency dependence for dispersive recombination with $\alpha = 0.6$ (black) and $\alpha = 0.4$ (blue). b) PA intensity dependence for monomolecular (green), bimolecular (red) and combined mono- and bimolecular recombination (black), assuming dispersion with $\alpha = 0.6$. The inset shows the intensity dependence for bimolecular recombination at low excitation intensity. Both a) and b) are modeled after equations (2.11) and (2.12). Solid curves correspond to the inphase- and dashed curves to the quadrature components of the PA. The calculations have been done using $\tau = \beta = \sigma = d = 1$, as well as $G = 1$ in a) and $\omega = 1$ in b).

low excitation intensity PA_I and PA_Q show $G^{(1+\alpha)/2}$ dependence, and at high excitation intensity PA_I approaches square root dependence, whereas PA_Q shows $G^{1/(2(1-\alpha))}$ dependence [61]. These dependences are presented in Figure 2.4 b).

2.1.4 Lifetimes from the phase information

When measuring cwPA spectra, both the inphase and the quadrature signal are recorded. Thus the phase spectra can be studied to gain information about lifetimes for excitations contributing to different parts of the PA spectra. A longer lifetime will reduce the PA_I/PA_Q ratio, which when the signal is represented in polar coordinates gives more negative phase, ϕ, as

described by equation (2.6).

Mathematically, the phase is given by

$$\phi(\omega) = -\arctan(\omega\tau_0) \tag{2.13}$$

for nondispersive excitations (one distinct lifetime), or by

$$\phi(\omega) = -\arctan\left(\frac{\sin(\frac{\pi}{2}\alpha)(\omega\tau_0)^\alpha}{1+\cos(\frac{\pi}{2}\alpha)(\omega\tau_0)^\alpha}\right) \tag{2.14}$$

for dispersive excitations. Solving for the effective lifetime τ_0 from the equations (2.13) and (2.14), we get

$$\tau_0 = \omega^{-1}\tan(-\phi) \tag{2.15}$$

for non-dispersive and

$$\tau_0 = \omega^{-1}\left(\frac{\sin(-\phi)}{\sin(\frac{\pi}{2}\alpha+\phi)}\right)^{1/\alpha} \tag{2.16}$$

for dispersive recombination, respectively.

Often, however, more than one kind of excitation absorbs at the same wavelength. This causes the PA signals from the various excitations to mix, giving an effective total PA signal (PA_{tot}) and an effective total phase (ϕ_{tot}). This results in inaccuracies in the lifetimes calculated by the equations above. For two excitations overlapping, $PA_{tot} = PA_{1R}e^{i\phi_1} + PA_{2R}e^{i\phi_2} = PA_{Rtot}e^{i\phi_{tot}}$, where ϕ_{tot} can be shown to be

$$\phi_{tot} = \arctan\left(\frac{PA_{1R}\sin\phi_1 + PA_{2R}\sin\phi_2}{PA_{1R}\cos\phi_1 + PA_{2R}\cos\phi_2}\right). \tag{2.17}$$

For $PA_{1R} = PA_{2R}$, ϕ_{tot} will be the average of ϕ_1 and ϕ_2, whereas a larger PA_{1R} (PA_{2R}) will shift ϕ_{tot} closer to ϕ_1 (ϕ_2), as intuitively expected.

Other error sources include experimental errors and noise in the data. These can be amplified if too low a modulation frequency ($\omega\tau_0 \ll 1$) is chosen, making the PA_Q component close to zero. The phase is rarely

studied in literature, but even with its limitations it is a useful tool for distinguishing between excitations in the PA spectra, and finding approximate lifetimes. For a more exact determination of the excitation lifetimes, the modulation frequency dependence of the PA can be measured, and fitted using either equations (2.7) and (2.8) (no dispersion) or (2.11) or (2.12) (with dispersion).

2.2 Transient photoinduced absorption

Transient PA probes the decay of photoexcitations generated by a short excitation pulse as a function of time. In the time domain, mathematical analysis is much simpler, and analytical solutions can be found for a broader set of equations.

Taking equation (1.6), assuming a depth profile for n(0) that follows Lambert-Beer's law, $n(x, t = 0) = \exp(-\alpha_L x)$, and integrating over the sample thickness d yields a general expression for the PA decay in the time domain:

$$PA(t) = \frac{AQ(t)}{P(t)} \ln\left(\frac{1 + P(t)}{1 + P(t)e^{-\alpha_L d}}\right), \tag{2.18}$$

where $Q(t)$ and $P(t)$ are given by equations (1.7) and (1.8), respectively, and $A = \frac{n(0)\sigma}{\alpha_L}$ [62]. This equation can be used for modeling both mono- and bimolecular recombination with arbitrarily chosen time dependences for $k(t)$ and $\beta(t)$, and thus accounts for both non-dispersive and dispersive recombination.

Chapter 3

Experimental

3.1 Materials

The most common model system for an organic solar cell donor polymer is poly(3-hexyl thiophene) (P3HT) (Figure 3.1 a)) [76]. P3HT has been widely studied and is readily available in various degrees of purity and side chain order. In this work, two subtypes of P3HT are discussed, namely regioregular-poly(3-hexyl thiophene) (rr-P3HT) and regiorandom-poly(3-hexyl thiophene) (rra-P3HT). These two differ from each other in side chain order. Rr-P3HT has regular head-to-tail coupling, showing a highly ordered fishbone-like orientation of the side chains [77]. Because of this order, rr-P3HT chains can stack on top of each other and form lamellar, crystalline structures [34, 78–81]. Rr-P3HT-based solar cells are known to show a reduced recombination of charges compared to many other polymers and consequently perform reasonably well [11,82]. Rra-P3HT on the other hand has randomly oriented side chains, which prevent the rra-P3HT chains from stacking, and performs poorly as a solar cell material. The stacking of rr- and rra-P3HT is illustrated in Figure 3.2. Being chemically similar but structurally and morphologically different, these two polymers are an interesting system for examining the influence of structure and morphology on photophysical properties and electronic processes in solar cell active layers [83].

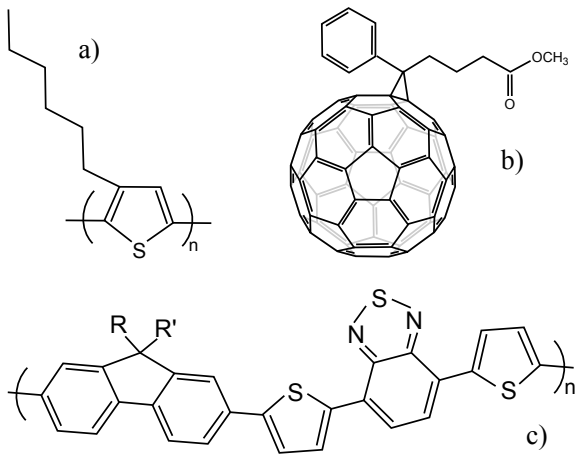

Figure 3.1: Structures of the main molecules discussed in this work. a) P3HT, b) PCBM, c) APFO3.

The acceptor material most commonly used in organic solar cells is the fullerene derivative [6,6]-phenyl-C_{61}-butyric acid methyl ester (PCBM). Compared to fullerenes, which are relatively insoluble, the functionalized PCBM is readily soluble in many common organic solvents. The structure of the molecule is presented in Figure 3.1 b).

The alternating polyfluorene copolymer, poly [2,7-(9,9-dioctyl-fluorene)-*alt*-5,5-(4',7'-di-2-thienyl- 2',1',3-benzo-thiadiazole)] (APFO3), see Figure 3.1 c), has been synthesized by Prof. Mats Andersson at Chalmers Technical University, Sweden. The polymer was designed to have an internal donor-acceptor structure between the alternating repeat units with different electron affinity. Semiempirical quantum-chemical calculations indicate that the first excited state S_1 has charge transfer character, with electron transfer taking place from the thiophene and fluorene units to the benzothiadiazole units, while the hole is delocalized on the π-conjugated backbone [84]. Advantages of APFO3-based solar cells include a relatively high open circuit voltage of 1 V [21], and decent power conversion efficiency of

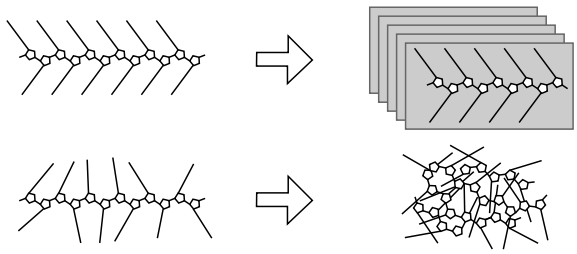

Figure 3.2: Difference in stacking between rr- and rra-P3HT.

3.5 % [13]. The internal donor-acceptor character is intriguing, as it may facilitate separation of excitons into charges. This category of polymers also show extended absorption in the red part of the visible spectrum [85]. In this work the P3HT and APFO3 polymers are studied both independently and in blends with PCBM.

3.2 Continuous wave photoinduced absorption

The majority of the measurements presented in this work have been carried out using the continuous-wave PA measurement system at the Department of Natural Sciences / Physics at Åbo Akademi University. The cwPA setup uses an Argon ion (Ar^+) laser for 514 nm and 355 nm excitation, modulated by either a mechanical chopper or an acousto-optical modulator and focused on a 0.18 cm^2 or 0.25 cm^2 area on the sample (defined by a mask), depending on the optics used. For photoexcitation at 785 nm wavelength, a diode laser (Power Technology PMT(785-50)) is used. The sample is mounted within a cryostat (Oxford Optistat Bath or Janis Research VPF-475), where the temperature can be controlled between 80 and 300 K. A tungsten projector lamp, often with a 610 nm cutoff filter, serves as a probe light and is focused on the same area of the sample as the excitation light using a spherical mirror. The transmitted probe light is collected by another spherical mirror and focused into a monochromator (Acton Research

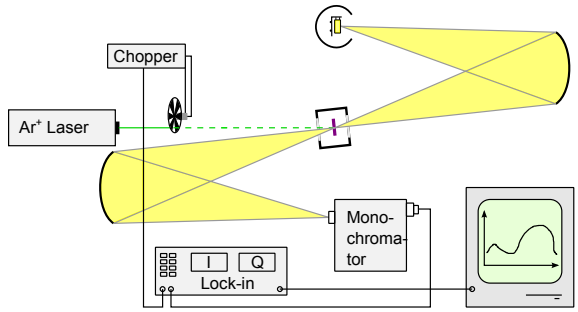

Figure 3.3: Schematic drawing of the cwPA setup

Corporation 300i) with appropriate cutoff filters and gratings. Finally, Si, Ge and InSb detectors are connected via a preamplifier (EG&G Optoelectronics PA-7-44) to a lock-in amplifier (Stanford Research SR830 DSP) to measure the photoinduced absorption of the sample. A schematic of this setup can be seen in Figure 3.3. Luminescence can overlap with the PA signal and is measured in a similar way as ΔT but with the probe light blocked. The obtained luminescence is then subtracted from the ΔT signal containing mixed PA and luminescence data. For excitation intensity dependence measurements, the Ar^+ laser is set to maximum desired intensity and a set of absorption filters are used to vary the intensity of the light on the sample.

3.3 Transient photoinduced absorption

Transient PA on femto- to nanosecond timescales was measured at Lund Laser Centre, an European large scale facility, using their ultrafast pump-probe setup. The measurement system was based on a pulsed Ti:sapphire laser (Clark-MXR, CPA-2001), from which both excitation and probe pulses were generated using noncollinear optical parametric amplifiers (NOPA). The pump light was set to 570 nm, and the probe light to 975 nm or 775 nm. A long delay line on the probe pulse, together with a pulse width of $\sim$

50 fs, allowed for straightforward measurements in the 100 fs - 10 ns time range. The probe light was measured using Si photodiodes. A continuous gas flow cryostat (Oxford, Optistat^{DN}) was used to control the temperature of the samples between 80 and 300 K.

Measurements in the micro- to millisecond time range were done using a flash photolysis setup, where a pulsed laser (Spectra-physics Quanta-Ray Pro230-10/MOPO-710) running at 355 nm and with a pulse width of 7 ns and a repetition rate of 10 Hz was used for exciting the sample. A 75 W xenon white light arc lamp served as probe light, and was focused inside the excited area of the sample. The transmitted probe light was collected into a monochromator and detected with a photo multiplier tube (PMT), after which the signal was amplified and digitized by a transient recorder. The signal noise was reduced by averaging the measured transients over several laser pulses. The setup is discussed in more detail elsewhere [86].

3.4 Delayed fluorescence

Delayed fluorescence (DF) measurements were carried out at the Department of Physics, Durham University. For the DF measurements, an yttrium aluminum garnet (YAG) laser operating at 355 nm was used as the excitation source. The resulting luminescence was measured using a spectrograph and a gated, intensified charge coupled device (CCD) detection system. The sample, a freshly spin-coated APFO3 sample on a sapphire substrate, was kept at 80 K during the measurement. Time dependence of the luminescence was measured by varying the delay time between the excitation pulse and the light collection, as well as the integrating time of the CCD. This method is explained in detail elsewhere [87].

Chapter 4

Results and discussions

4.1 Characterization of long-lived excitations in APFO3:PCBM blends

The absorption and photoluminescence spectra of the neat APFO3 as well as for blends with PCBM in 1:4 and 4:1 ratios are presented in Figure 4.1. All three films show an onset of absorption at roughly 2 eV. The two featureless absorption bands of APFO3 at 2.30 and 3.22 eV have been assigned to the first singlet state and a $\pi - \pi^*$ transition, respectively [84]. Addition of PCBM decreases the magnitude of these bands, and at the same time a third absorption band due to PCBM absorption appears at 3.70 eV. The photoluminescence, clearly visible for the neat APFO3, is strongly quenched by addition of PCBM, which correlates well with efficient exciton splitting [17]. The remaining redshifted PL can be attributed to PCBM luminescence, as discussed in Papers I – II.

Photoinduced absorption spectra and phase spectra for the three films at 80 K and room temperature are presented in Figure 4.2 a) and b), respectively. The PA spectra are qualitatively similar in shape, with a low energy absorption band at $\sim$ 0.35 eV, and a high energy absorption band roughly between 1 and 2 eV. The neat APFO3 and the blend with 20% APFO3 show similar overall PA amplitudes at 80 K, whereas the overall PA amplitude for the blend with 80% APFO3 is roughly 2.5 times

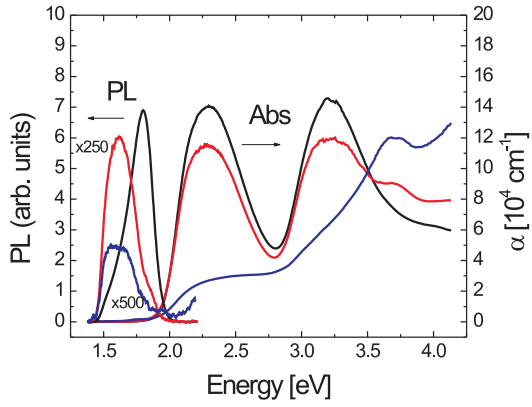

Figure 4.1: Absorption and photoluminescence spectra for neat APFO3 (black line) and blends with PCBM in 4:1 (red line) and 1:4 (blue line) weight ratios.

higher. For all three films, the low energy absorption band is assigned to the P1 optical transition of polarons, and a corresponding portion of the high energy absorption band at $E_{gap} - 2P1 = 1.3$ eV to the correlated P2 optical transition. The majority of the high energy band is of another origin, which is evident from the phase spectra in Figure 4.2 a) and b). The second excitation appears to have a stronger temperature dependence than the polarons, and at room temperature only a polaron P2 peak can be observed at ~ 1.35 eV, in good agreement with where it is expected to be (1.3 eV). The amplitude of the polaron signal at room temperature is largest for the blend with 20% APFO3, which is also the blend showing highest power conversion efficiencis in actual devices [85].

Looking at the 80 K phase data, we observe the following. The low energy P1 band for all three films shows significantly larger absolute phase values than the high energy band, suggesting that the high energy band is dominated by an excitation with a shorter lifetime than the polarons. We expect to have the P2 transition of polarons at ~ 1.3 eV and in the phase

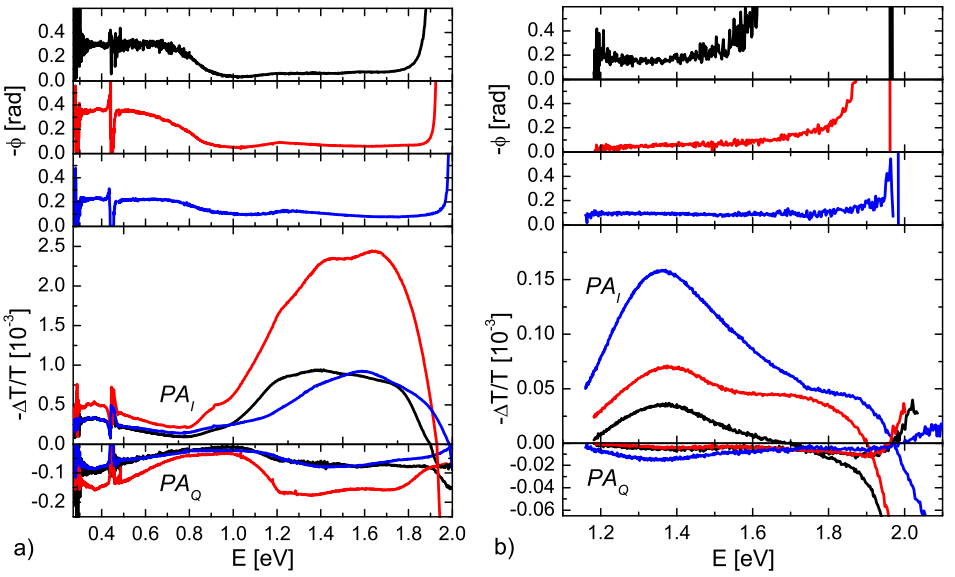

Figure 4.2: Photoinduced absorption spectra (both PA_I and PA_Q components) for the APFO3:PCBM 1:0 (black), 4:1 (red) and 1:4 (blue) blends, together with the corresponding phase values measured at a) 80 K and b) room temperature.

spectra of the blends we can indeed observe a bump at around 1.25 eV. Phase data at room temperature shows no indication of multiple lifetimes, consistent with only polarons being present at room temperature. However, the phase spectra at room temperature were not measured at low enough energy to observe the P1 peak, making the analysis of the phase less useful.

Besides polarons, one of the most common long lived excitations in conducting polymers are triplet excitations. Therefore, it would be tempting to at least partially assign the unknown high energy band in the case of neat APFO3 to triplet excitons. However, no phosphorescence could be detected and from the similarity of the spectra it seems that the unknown excitation prevails after adding PCBM. This is a strong indication against triplet exci-

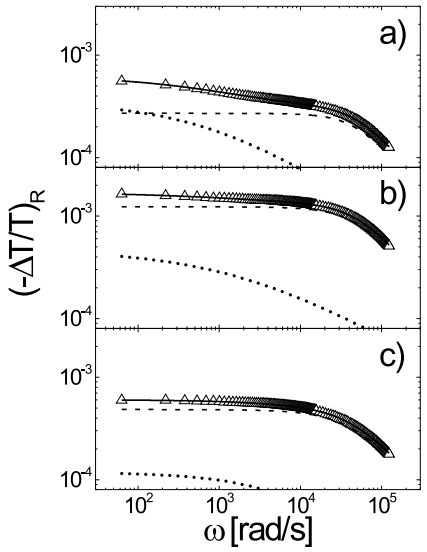

Figure 4.3: Frequency dependences of the PA_R signal for the APFO3:PCBM 1:0, 4:1 and 1:4 blends. Fits using equation (2.10) for two components are plotted as solid lines and the components of the fits are shown with dashed and dotted lines.

tons, as excitons are known to be efficiently quenched by fullerenes [88, 89]. Another type of excitation that would fit the observed spectral characteristics is polaron pairs, as they have a blue(red)-shifted PA band relative to the P2(P1) transition and have been observed in closely related materials [36]. Furthermore, at room temperature the lifetime of polaron pairs has been found to be in the ns time regime, which makes them too short lived to be observed with our cwPA setup [90]. Thus we tentatively assign the high energy PA band in both neat APFO 3 and the blends with PCBM to a superposition of polarons and polaron pairs.

To discover the lifetimes and dispersion parameters of our two excitations, we measured modulation frequency dependence for the PA on top

Table 4.1: Lifetimes and dispersion parameters extracted from frequency dependence fits.

	APFO3	APFO3:PCBM 4:1	APFO3:PCBM 1:4
τ_1^* (fast) [μs]	19	20	24
α_1 (fast)	0.98	0.95	0.89
τ_2^* (slow) [ms]	1.4	0.57	0.15
α_2 (slow)	0.51	0.46	0.62

of the HE band at 80 K. Excitation modulation frequency was varied over several orders of magnitude and the obtained PA response is shown in Figure 4.3. Fitting for two components using equation (2.10) revealed a short-lived nondispersive component and a long-lived, dispersive component in all three films. The values for all three films are presented in Table 4.1. We assign the slow, dispersive component to polarons, and the fast, nondispersive component to polaron pairs. In the case of the blends, the slow component is less pronounced, increasing the error margin for those parameters.

To check the usability of phase data for lifetime evaluation, lifetimes for the polaron (slow) component in all three blends at both 80 K and room temperature were calculated from the phase data using equation (2.16), and are presented in Table 4.2. Dispersion parameters for the calculations were taken from the frequency dependence fit. The lifetimes obtained in this way correspond fairly well with the frequency dependence lifetimes, showing that the phase data can be used in a convenient way to find the directional lifetimes of dominant excitations in the PA spectra, provided the dispersive behavior is known.

As a final sanity check, μs to ms transient decays were measured on the neat APFO3 film and the blend with 20 % PCBM. The results are shown in Figure 4.4. Fitting with a two-component exponential decay equation, which assumes monomolecular recombination and does not take dispersion effects into account (see Table 1.1), revealed lifetimes of 19 μs (4.0 ms)

Table 4.2: Lifetimes for polarons at 80 K and at room temperature, as calculated from the phase values.

	APFO3	APFO3:PCBM 4:1	APFO3:PCBM 1:4
$\tau^*_{polaron}$ (80 K) [ms]	0.6	1.3	0.2
$\tau^*_{polaron}$ (293 K) [μs]	75	8	38

in neat APFO3 and 20 μs (2.7 ms) in the blend with 20% PCBM for the fast (slow) component. Although the monomolecular model was chosen for simplicity, these numbers are in agreement with those from the frequency dependence and phase measurements. Intensity dependence measurements in Paper II suggest that the recombination mechanism at high excitation intensities is mainly bimolecular in nature.

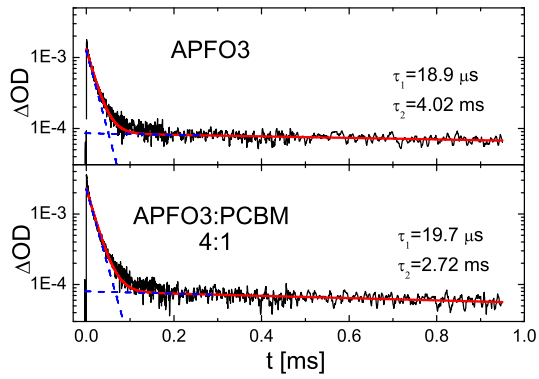

Figure 4.4: Transient PA decays for neat APFO3 and APFO3:PCBM 4:1. The red curve is a fit using two exponential functions and the blue dashed lines represent the individual exponentials.

4.2 Modeling transient PA decays in APFO3

The built in charge transfer character of APFO3 and the promising results it shows in solar cell devices called for an in-depth study of the photoexcitation processes in APFO3. In Paper III, the photogeneration and recombination of excitations and charges on femtosecond to nanosecond timescales in APFO3 are studied using transient PA and time resolved delayed fluorescence. A series of PA measurements at 80 K using different excitation intensities are presented in Figures 4.5 and 4.6 for probe wavelengths of 975 nm (1.27 eV) and 775 nm (1.6 eV), respectively. Furthermore, delayed fluorescence was measured on nano- to microsecond timescale, and is presented in Figure 4.7.

The transient PA decays for the neat APFO3 film were measured from 100 fs to 10 ns, using a range of excitation intensities from 0.17×10^{14} to 6.5×10^{14} photons/cm^2. At 975 nm we see that the decay of the PA signal becomes faster with increasing excitation intensity (see Figure 4.5), indicating a bimolecular recombination process. At the longest times we can observe the decay dynamics approaching a constant value, most clearly seen for the highest excitation intensities used. This suggests that another excitation with a significantly longer lifetime contributes to the PA signal at 975 nm. The inset in Figure 4.5 shows that the intensity dependence of the PA signal at 0.2 ps is linear, which agrees well with an assignment of the main (fast) component to singlet excitations.

Looking at the results for 775 nm excitation in Figure 4.6, we also see clear evidence of two different components, although the behavior of these components is different from those at 975 nm. There is an initial fast (compared to 975 nm data) decay followed by a slow buildup starting from $\sim$ 100 ps. This is most evident at the lowest excitation intensities. The fast initial decay has previously been assigned to geminate recombination of intrachain polaron pairs [91,92]. The intensity dependence of the PA at 0.5 ps (Figure 4.6 inset) shows an approximately linear relation, suggesting that the intrachain polaron pairs have been created from singlet excitons. We attribute the fast recombination in Figure 4.6 to geminate recombination of intrachain polaron pairs back to singlet excitons, contributing to the signal

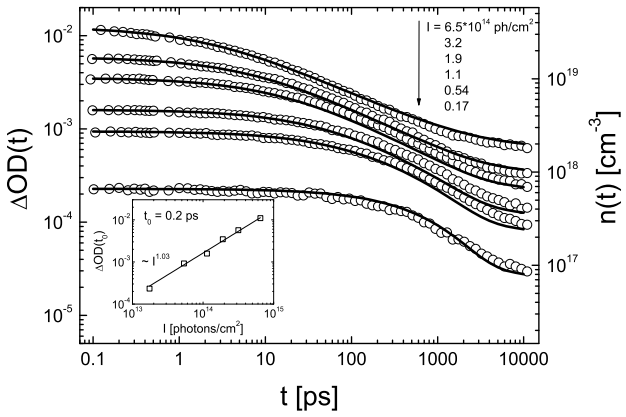

Figure 4.5: Transient PA dynamics of the PA band at 1.27 eV (975 nm) in APFO3 for different pump intensities, measured at $T = 80$ K using the pump wavelength $\lambda_{pump} = 570$ nm (2.18 eV). The solid lines are numerical fits to the rate equation model presented in this chapter. The photoexcitation concentration $n(t)$ on the y-axis to the right is directly related to $\Delta OD(t)$ via the relation $n(t) = (\ln 10\ \alpha_L/\sigma) \times \Delta OD(t)$, where $\alpha_L(570nm) = 1.26 \times 10^5$ cm^{-1} and $\sigma = 10^{-16}$ cm^2. The pump intensity dependence of the PA band taken at $t = 0.2$ ps is shown as an inset, and the solid line is a fit to PA $\sim I^{\delta}$, yielding $\delta \approx 1.03$.

measured in Figure 4.5. This is supported by the fact that recombination of polaron pairs is likely to happen via the singlet exciton state. Also, dissociation of the polaron pair to free polarons would not yield a significant change in the PA, as both polarons and polaron pairs tend to absorb in this wavelength region. The slow component buildup occurs on the same timescales as the singlet exciton decay observed at 975 nm, suggesting that the buildup could be formed from singlet excitons via EEA. As to the nature of the excitation building up, it has been suggested that the EEA process produces polaron pairs that are mainly of interchain type, i.e. with the charges residing on adjacent polymer chains [32]. Both intra- and interchain

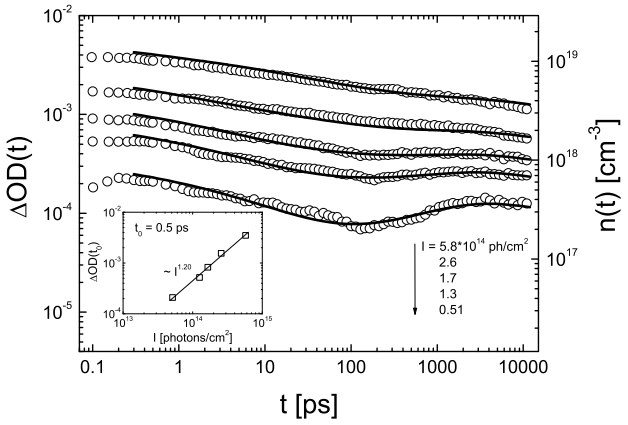

Figure 4.6: Transient PA dynamics of the PA band at 1.6 eV (775 nm) in APFO3 for different pump intensities, measured at $T = 80$ K using the pump wavelength $\lambda_{pump} = 570$ nm (2.18 eV). The photoexcitation concentration $n(t)$ on the right y-axis is directly related to $\Delta OD(t)$ via the same relation as in Fig. 4.5. The solid lines are numerical fits to the rate equation model presented in this chapter. The pump intensity dependence of the PA band taken at $t = 0.5$ ps is shown as an inset and the solid line is a fit to PA $\sim I^{\delta}$, yielding $\delta \approx 1.20$.

polaron pairs are expected to absorb in the same wavelength region. All of this is in agreement with the assignment of the buildup to interchain polaron pairs.

The delayed fluorescence, shown in Figure 4.7, extends over five orders of magnitude in time and shows two components, a fast component on nanosecond timescales, and a slow, dispersive, component on microsecond timescales. The fast component is attributed to prompt fluorescence of the singlet excitons. Delayed fluorescence in conjugated polymers is typically assigned to either bimolecular triplet-triplet annihilation or polaron (pair) recombination [93–96]. As no evidence for triplet excitons could be found, we assign the slow DF component to recombination of polaron pairs back

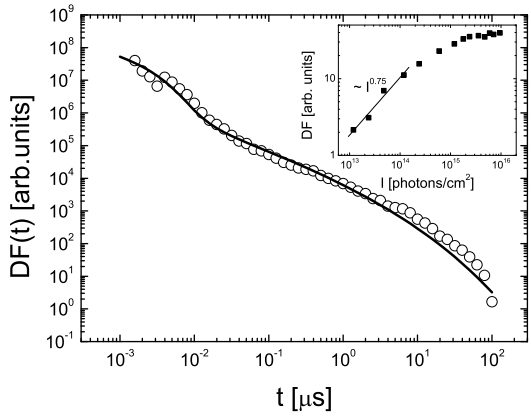

Figure 4.7: Time-resolved decay of the delayed fluorescence at 680 nm in APFO3. Measured at $T = 80$ K using the excitation wavelength $\lambda_{exc} = 355$ nm (3.50 eV). The excitation intensity dependence of the DF amplitude taken at 0.13 μs is shown in the inset. The solid line is a numerical fit to the rate equation model presented in this chapter. The solid line in the inset is a fit to DF $\sim I^{\delta}$, yielding $\delta \approx 0.75$.

to singlet excitons, and their subsequent radiative decay back to the ground state.

To model the dynamics in Figures 4.5, 4.6 and 4.7, the following hypotheses were made based on literature and experimental results:

1. Initially, vibronically excited singlet excitons are formed. These relax in part to the lowest energy singlet exciton state S_1, and in part dissociate into Coulombically bound intrachain polaron pairs PP_1.

2. The relaxed singlet excitons either recombine radiatively back to the ground state with a monomolecular rate k_{rad}, or dissociate with a certain probability into interchain polaron pairs PP_2 with a monomolecular rate k_{spp2}.

3. At higher pump intensities singlet excitons annihilate via EEA, generating higher energy excitons (S_n^*) with a rate B_{EEA}. A fraction of these high-energy excitons relax back to S_1, and the rest dissociate into interchain polaron pairs PP_2. These decay channels are represented with the bimolecular recombination coefficients B_{SS} and B_{spp2}, respectively. B_{EEA} is thus substituted by $(B_{ss} + B_{spp2})$. This recombination is also found to be of a dispersive character, with the dispersion coefficient γ_{ss}.

4. The intrachain polaron pairs PP_1 recombine geminately back to singlet excitons with a monomolecular recombination rate A_{pp1s} and dispersion coefficient α_{pp1s}.

5. Interchain polaron pairs PP_2 have several recombination channels. A large fraction is likely to recombine nonradiatively to the ground state or separate into free polarons with a monomolecular recombination coefficient of A_{pp20}, whereas the rest recombines back to singlet excitons with a monomolecular rate A_{pp2s}, causing delayed fluorescence. Polaron dynamics are not included in our model, as polaron generation and recombination is assumed to happen on longer timescales, outside of our observation window. The included recombinations are dispersive, with a common recombination coefficient α_{pp2s}.

The model is presented schematically in Figure 4.8, and expressed as rate equations, we get:

$$\begin{aligned}\frac{dS_1}{dt} &= -(k_{rad} + k_{spp2})S_1 - (B_{ss} + B_{spp2})t^{\gamma_{ss}-1}S_1^2 \\ &\quad + A_{pp1s}t^{\alpha_{pp1s}-1}PP_1 + A_{pp2s}t^{\alpha_{pp2s}-1}PP_2 \end{aligned} \tag{4.1a}$$

$$\frac{dPP_1}{dt} = -A_{pp1s}t^{\alpha_{pp1s}-1}PP_1 \tag{4.1b}$$

$$\frac{dPP_2}{dt} = k_{spp2}S_1 + B_{spp2}t^{\gamma_{ss}-1}S_1^2 - (A_{pp2s} + A_{pp20})t^{\alpha_{pp2s}-1}PP_2 \tag{4.1c}$$

Table 4.3: Summary of parameters used in modeling the recombination dynamics of APFO3.

Parameter	Value	Unit
k_{rad}	5.0×10^8	s^{-1}
k_{spp2}	2.0×10^8	s^{-1}
A_{pp1s}	200	$s^{-\alpha_{pp1s}}$
A_{pp20}	26.7	$s^{-\alpha_{pp2s}}$
A_{pp2s}	1.2	$s^{-\alpha_{pp2s}}$
B_{ss}	1.6×10^{-13}	$cm^3/s^{\gamma_{ss}}$
B_{spp2}	2.1×10^{-14}	$cm^3/s^{\gamma_{ss}}$
α_{pp1s}	0.25	
α_{pp2s}	0.3	
γ_{ss}	0.6	

The experimental curves were modeled using equations 4.1a, 4.1b and 4.1c, and the results can be seen as solid lines in Figures 4.5 and 4.6. Further, the delayed luminescence in the μs regime following excitation with 355 nm (3.5 eV) light was modeled using the same model as for the tPA results, as it is proportional to the S_1 concentration. These results are shown in Figure 4.7. All curves measured at different excitation intensities and the delayed luminescence could be modeled using one set of parameters, presented in Table 4.3.

The model above is an attempt to explain our experimental results in the simplest possible way, with just enough complexity to explain observed features and with a minimum degree of freedom. There may be, however, other processes and parameters that can explain our results equally well. Most notably, the two different polaron pairs that are used to distinguish between a fast and a slow excitation decay may, in light of recent discussions about CT states, be assigned differently. The model above can not be seen as a universal model for conducting polymers or even polymers for solar cell applications, but may give some insights into the dynamics of other

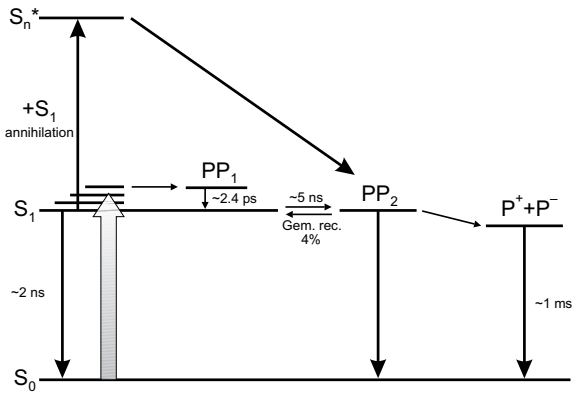

Figure 4.8: Schematic diagram of the formation and recombination channels of photoexcitations in APFO3.

polymers with a similar donor-acceptor character.

The link between these ultrafast neat APFO3 results and the micro-millisecond timescale results in Section 4.1 may not be immediately clear, as free charges are not directly included in the rate model above. A fraction of the interchain polaron pairs PP_2 in the model will separate into free polarons, presumably on nano- microsecond timescales, and recombine dispersively on millisecond timescales, as observed and discussed in Section 4.1. Looking at the delayed fluorescence in Figure 4.7, we can observe what appears to be an end of the dispersive behavior on the timescale of tens of microseconds. Thus, it is possible that the polaron pairs that recombine non-dispersively with a lifetime of 20 μs in the cwPA measurements can be identified with the edge of the lifetime distribution for the interchain polaron pairs PP_2 in the model above.

4.2.1 Ultrafast photophysics in APFO3:PCBM

For a more complete picture of the photophysical processes in APFO3, it is also important to look at the ultrafast processes in the APFO3:PCBM

blend. Based on our results for the neat APFO3, De et al. have modeled the dynamics in the APFO3:PCBM blend on femto- to microsecond timescales at room temperature [97,98]. They have used a similar approach as presented above for APFO3, with global fitting of a rate model to transient PA data measured over almost 2 orders of magnitude in excitation intensity and up to nine orders of magnitude in time. Their main findings are the following. Addition of PCBM in concentrations higher than 20 % by weight results in a separation of the initial excitons into bound charge pairs on the $\sim$ 200 fs timescale. This is evidenced both by a quenching of the fluorescence and a decay in the picosecond PA transients. This agrees well with our photoluminescence measurements in Figure 4.1. On the $\sim$ 30 ps timescale, there is a rise in the transient PA signal, which De et al. assign to formation of free charges. This is followed by recombination of the free charges on the nano- microsecond timescales. If the PCBM concentration is gradually decreased, generation of separated charges becomes less and less efficient and the PA transient shape approaches that in Figure 4.5 for neat APFO3 [98], but with faster decay due to the higher temperature of the sample.

The results in Papers I and II describe the photophysics of the long-lived charges. Due to the difference in temperature, a direct comparison between the ultrafast results by De et al. and the cwPA results requires careful consideration. De et al. observed nondispersive geminate recombination as the dominating recombination mechanism for free charges, with dispersive bimolecular recombination increasing in importance at higher excitation intensities. This agrees well with the intensity dependence data presented in Paper II, showing a change from monomolecular to bimolecular recombination as the excitation intensity is increased. The main weakness of the APFO3:PCBM blend is thus a significant monomolecular recombination competing with the charge extraction at solar illumination intensities. The polaron recombination discussed in Papers I and II was obtained using high excitation intensity and therefore the observed dispersive character of the polarons is fully in agreement with the ultrafast studies by De et al. The polaron pairs with a 20 μs lifetime observed in Figure 4.2 a) and in the related measurements are likely the same as the bound charge pairs with

a lifetime of 30 ps observed by De et al.. They are both nondispersive in nature, and the extension of the lifetime in the cwPA measurements can be explained by the lower temperature used. This is also supported by the PA spectra at 80 K and 293 K in Figure 4.2 a) and b), showing how the polaron pairs disappear when the temperature is increased. Thus we can conclude that the results of De et al. complement our work in Papers I and II nicely.

4.3 Charge transfer and dipole formation in the P3HT:PCBM bulk heterojunction

Annealed P3HT:PCBM solar cells are well known to exhibit a reduced recombination of charges compared to most other polymer:PCBM systems [11, 82], including APFO3:PCBM. This makes it an interesting reference system to study, especially as the reason for the reduced recombination is still not fully understood. To probe the changes in the electronic structure of regioregular- and regiorandom-P3HT polymers as a result of annealing, UPS measurements were performed by Parisa Sehati and Slawomir Braun at Linköping University and the results were interpreted using the integer charge transfer (ICT) model [99–101]. The UPS technique probes the ionization potential (IP) of the bulk of the film, which is a measure of the electronic part of the polaronic relaxation energy and screening effects from the surrounding medium. The geometric relaxation of the polymer is not included in the IP. Using a suitable substrate together with the polymer films, the ICT model together with the UPS data was used to determine the energy of the positive integer charge transfer states E_{ICT+}, which correspond to a fully relaxed (i.e. both electronic and geometric relaxation) hole polaron state on the polymer. The ICT states correspond to the most relaxed polaron states close to the substrate/polymer interface. Thus, geometric relaxation of the polymer chain by a polaron, here called the vertical binding energy (VBE), is given by the difference between the IP and E_{ICT+}. These parameters are illustrated in relation to the HOMO and LUMO levels in Figure 4.9.

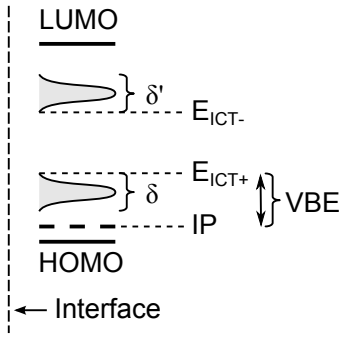

Figure 4.9: Schematic view of the IP, E_{ICT+}, and VBE with respect to the HOMO and LUMO levels. The δ' and δ represent the electron- and hole polaron energy distributions, respectively (not to scale or shape). The values for the E_{ICT+} and IP are measured in energy below the vacuum level.

The key results from the UPS measurements are presented in Table 4.4 and are interpreted as follows: Upon thermal cycling of rra-P3HT from room temperature to 150 °C and back to room temperature, we observe the well known thermochromic effect in polyalkylthiophenes [102,103]. Heating causes a decrease in the effective conjugation length of the molecules due to twisting of the thiophene rings. This can occur at sites distributed randomly in the bulk of the film, causing a decrease of the IP and an increase of the E_{ICT+} level. Cooling back to room temperature restores most of the twists on the chain (the IP changes back to the initial value), but some sites remain distorted, as evidenced by the permanent change of the E_{ICT+} level. The VBE in rra-P3HT is faily large (0.40 eV), reflecting the disordered nature of the polymer. The VBE is further increased by heating, and stays large at the sites where distortion is retained after cooling down. A schematic view of the effects of thermal cycling on both rra-P3HT and rr-P3HT is presented in Figure 4.10.

The initial VBE in rr-P3HT is only 0.1 eV due to the tendency of rr-P3HT to form lamellas, which collectively lock the chains in place. Thus,

Table 4.4: Values for E_{ICT+}, IP and VBE in rra- and rr-P3HT as a function of thermal cycling from room temperature (RT_i) up to 150 °C, and back down to room temperature (RT_f). The values for the E_{ICT+} and IP are measured in energy below the vacuum level.

	Rra-P3HT			Rr-P3HT		
	RT_i	150°C	RT_f	RT_i	150°C	RT_f
E_{ICT+} [eV]	4.30	4.05	4.05	4.40	4.05	4.00
IP [eV]	4.70	5.20	4.75	4.50	4.50	4.45
VBE [eV]	0.40	1.15	0.70	0.10	0.45	0.45

upon heating, there is no change in the IP. The E_{ICT+} level on the other hand, is shifted up in a similar way as for rra-P3HT due to thermochromic effects on chain ends, loops and loose chains at the edges and around the lamellas. After cooling back down to RT some of these sites remain distorted, as shown by the unchanged E_{ICT+} level.

We propose, using values obtained from the UPS measurements, that the E_{ICT+} level of the polymer can, after annealing, relax to sufficiently high energy (4.05 eV) so that an electron can spontaneously be transferred to the E_{ICT-} level of PCBM (4.2 eV [104]), forming a dipole at the interface. Once a dipole is present at the interface, separation of subsequent optically generated electron-hole pairs from the interface to free charges is enhanced due to reduced geminate recombination at the interface [105, 106].

To observe the effect of the interfacial dipoles we set up a series of PA measurements on both rr- and rra-P3HT:PCBM 1:1 blends, using both above- and below-gap excitation light (514 nm and 785 nm, respectively), before and after annealing of the film. While excitation of the neat polymers (Figure 4.11) only generates photoexcitations when using above-gap light, excitation of the polymer/fullerene blends (Figure 4.12) show generation of polarons using both above- and below-gap light. Annealing enhances the polaron generation in the regioregular P3HT:PCBM film, while the regiorandom P3HT:PCBM film shows no significant change in the polaron

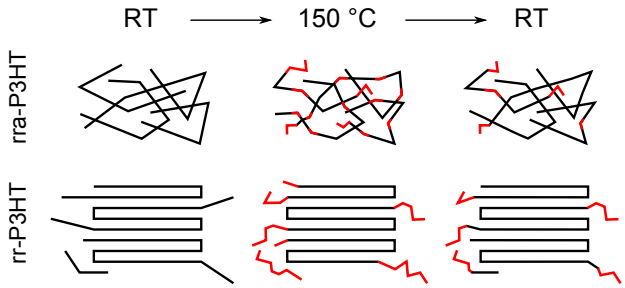

Figure 4.10: Schematic view of the effects of thermal cycling on rr- and rra-P3HT. The chain segments with increased disorder due to heating are coloured red.

concentration after annealing.

Using equation 2.15 (assuming no dispersion), we estimate the lifetimes of the polarons in the rra-P3HT:PCBM and rr-P3HT:PCBM blends. Steady state charge concentrations (n) are estimated from the high energy polaron absorption peak (P2) amplitudes in the PA spectra using $PA = n\sigma d$ from equation (2.2), assuming $\sigma = 10^{-16}$ cm^2. The values for the lifetimes and charge concentrations are presented in Table 4.5.

The charge densities and lifetimes in both rr-P3HT:PCBM and rra-P3HT: PCBM agree well with dipole formation at the polymer/fullerene interface upon annealing, as well as with the general characteristics of the polymers. The rra-P3HT:PCBM blend is disordered regardless of annealing and a strong localization of the polarons results in long lifetimes. The localization of separated charges largely negates the beneficial repelling effect of the introduced interfacial dipoles, as the charges can not easily move away from the interface. For above-bandgap excitation an increase in the lifetime can nevertheless be seen, probably as a result of the higher energy allowing for more movement in the surrounding energy landscape. The charge concentrations in the rra-P3HT:PCBM blend are unaffected by annealing, as the diffusion of excitations from the amorphous rra-P3HT region to the interfaces with PCBM remains poor and the separation of

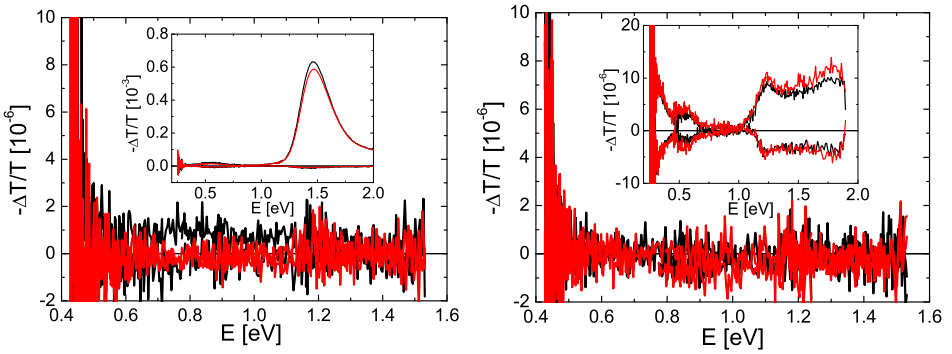

Figure 4.11: PA spectra of rra-P3HT (left) and rr-P3HT (right) using 785 nm excitation light, and 514 nm excitation light (insets). Spectra before annealing are shown in black, and after annealing in red. The in-phase and out-of-phase components assume positive and negative $-\Delta T/T$ values, respectively.

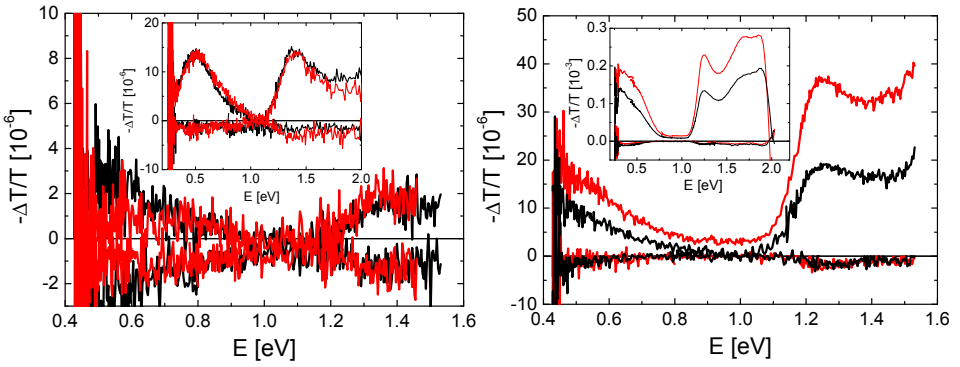

Figure 4.12: PA spectra of rra-P3HT:PCBM (left) and rr-P3HT:PCBM (right) using 785 nm excitation light, and 514 nm excitation light (insets). Spectra before annealing are shown in black, and after annealing in red. The in-phase and out-of-phase components assume positive and negative $-\Delta T/T$ values, respectively.

Table 4.5: Excitation lifetimes (τ) and charge concentrations (n) extracted from photoinduced absorption spectroscopy data for 785 and 514 nm excitation wavelengths. The values are measured at 1.4 eV and 1.25 eV probe energies (on top of the polaron P2 absorption peak) for rra-P3HT:PCBM and rr-P3HT:PCBM, respectively. Please note that the error margins given are only due to noise in the data.

	Rra-P3HT:PCBM		Rr-P3HT:PCBM	
	Unannealed	Annealed	Unannealed	Annealed
τ_{785} [μs]	1000(±300)	900(±300))	90(±30)	60(±20)
τ_{514} [μs]	170(±50)	280(±50)	70(±10)	35(±5)
n_{785} [10^{15} cm^{-3}]	0.7(±0.1)	0.9(±0.1)	4.6(±0.1)	9.0(±0.1)
n_{514} [10^{15} cm^{-3}]	4.8(±0.1)	4.8(±0.1)	149(±0.2)	255(±0.2)

charges away from the interface is not much improved by the interfacial dipoles. In rr-P3HT:PCBM the situation is different. There, we observe a significant increase in the charge concentration after annealing, indicating a reduced geminate recombination at the interface and improved separation of e-h pairs. This is consistent with the formation of an interfacial dipole. Lifetimes are much shorter than in rra-P3HT due to the higher order and consequently higher mobility in the blend, making bimolecular recombination the dominating recombination mechanism at high charge concentrations. As dipoles are introduced at the interfaces, the charge concentrations in the bulk increase and the lifetimes are further reduced due to bimolecular recombination. It is possible that the interfacial dipoles also act as a barrier for the non-geminate bimolecular recombination, but without knowledge about the blend microstructure and the preferred recombination sites it is difficult to tell. In Paper V, however, we take a closer look on the bimolecular recombination parameter β and it seems that the bimolecular recombination is unaffected by the interfacial dipoles.

Our strongest supporting argument (from the PA data) for the formation of interfacial dipoles comes from considering the morphological changes

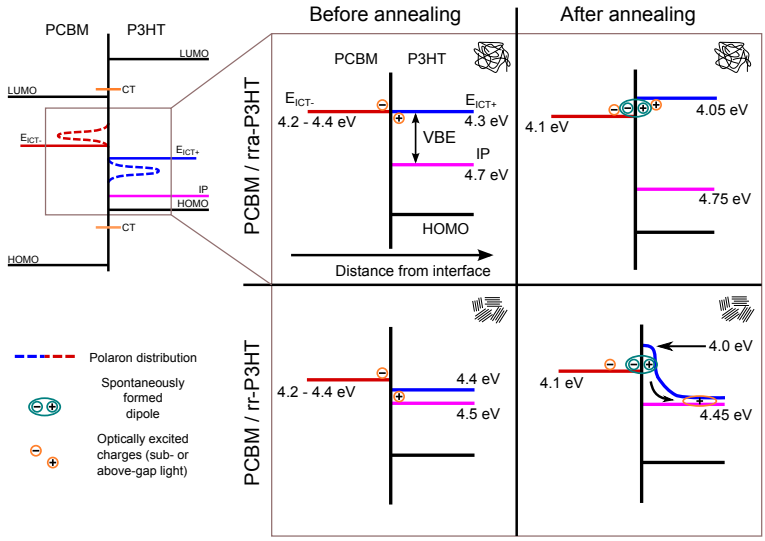

Figure 4.13: Schematic diagram of the ICT states in rr- and rra-P3HT before and after annealing. The dipole formation and charge separation from the P3HT:PCBM interfaces are also illustrated.

in the rr-P3HT:PCBM blend upon annealing and looking at the charge concentrations for sub-bandgap excitation in Table 4.5. It is well known that heat treatment of a rr-P3HT:PCBM film leads to improved order in the polymer phase and larger phase-separated regions. Consequently, it is expected that the interfacial area between the rr-P3HT and PCBM is reduced. Assuming that the sub-bandgap excitation light excites CT complexes at the P3HT:PCBM interfaces, it would be natural to see a reduction in the charge concentration after heat treatment, as there are less regions to excite in the film. Thus, to explain the observed increase in charge concentration, there has to be some driving force making the charge separation from the remaining CT complexes much more efficient. We suggest this is explained by the interfacial dipoles.

We suggest annealing induces dipoles at the P3HT:PCBM interface.

These reduce geminate recombination of separated electron-hole pairs and explain in part the high efficiency of the rr-P3HT:PCBM blend, which makes it one of the best model systems for efficient organic solar cells. A schematic view of the ICT states in rra-P3HT:PCBM and rr-P3HT:PCBM before and after annealing, as well as the suggested dipole formation and charge separation processes, are presented in Figure 4.13. Engineering new solar cell polymers to have controlled disorder at the edges of the lamellas for optimal interfacial dipole formation when mixed with PCBM might be a route for further improving polymer solar cell efficiencies.

4.4 Effect of heat treatment on bimolecular recombination in P3HT:PCBM blends

The results from the previous section raise the question how annealing affects the bimolecular recombination coefficient β in rr-P3HT:PCBM 1:1 blends. To find this, we measured the PA as a function of excitation intensity and the results for rr-P3HT:PCBM before and after annealing are shown in Figure 4.14 a) and b), respectively. The insets show the out-of-phase component plotted on a lin-log scale, with linear fits to the high intensity part of the data. Estimates of the bimolecular recombination coefficient were made from the slope of the linear fit. Using the relation $\beta = f\sigma d/slope$ from Equation (2.9), we obtained a β of 31×10^{-14} $\mathrm{cm^3 s^{-1}}$ for rr-P3HT:PCBM before annealing and 29×10^{-14} $\mathrm{cm^3 s^{-1}}$ after annealing. It thus seems, that for our films there is no net effect of the annealing and the thereby induced interfacial dipoles on the bimolecular recombination coefficient. The main effect of the interfacial dipoles is therefore a reduction of the geminate recombination during the initial charge separation at the P3HT:PCBM interfaces, leading to a higher charge generation efficiency of the annealed films, as shown in the previous section. As the theory for estimating β assumes no dispersion and requires essentially pure bimolecular recombination, it is more difficult to find β for rra-P3HT:PCBM in a reliable way, but the discussion has been included for completeness in Paper V.

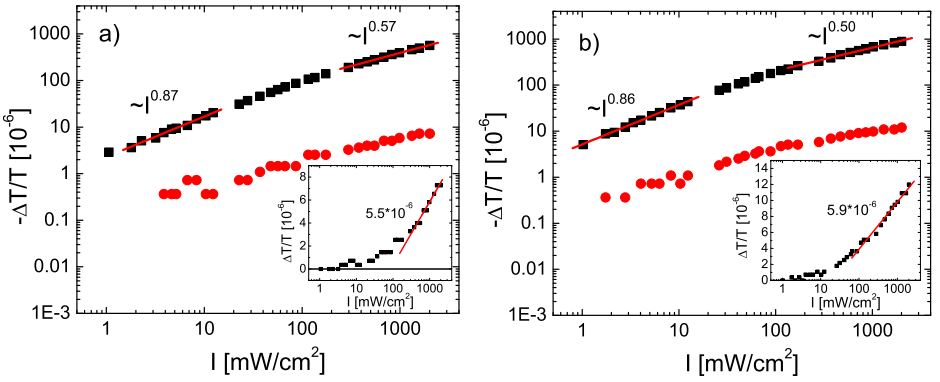

Figure 4.14: PA intensity dependence a) before and b) after annealing. The in-phase and out-of-phase components are plotted with black squares and red dots, respectively. The insets show the out-of-phase components plotted on a lin-log scale. Linear fits and slopes are included.

Chapter 5

Summary

In this work, photoinduced absorption techniques have been used in a number of ways to clarify the charge generation and recombination processes in two polymers used in organic solar cells, namely APFO3 and P3HT. Emphasis has been on identifying photoexcitations, modeling their dynamics and determining their lifetimes. Photoexcitation of neat APFO3 results in complex dynamics on fs – μs timescales, involving singlet excitons and both inter- and intrachain polaron pairs. Charges are formed as a result of polaron pair splitting on ns – μs timescales, and are shown to recombine dispersively with a lifetime of $\sim$ 1 ms. Mixing PCBM with APFO3, a rapid quenching of the luminescence is observed, attributed to efficient charge separation. Polarons and polaron pairs are observed both in neat APFO3 and APFO3:PCBM blends on μs – ms timescales with very similar behavior in both systems. This similarity may be explained by the internal donor–acceptor character of the APFO3 polymer. Phase data of the cwPA spectra was shown to be a useful tool for distinguishing between different long-lived excitations and estimating their lifetimes. All these results are found to be in perfect agreement with ultrafast measurements on APFO3:PCBM blends by De et al. and together they form a comprehensive picture of the photoexcitation dynamics in APFO3 based systems.

Mobile charges are generated in the rr-P3HT:PCBM blend using both above- and below-bandgap photoexcitation. In rra-P3HT:PCBM similarly

generated charges remain localized due to the disordered nature of rra-P3HT. UV photoelectron spectroscopy measurements indicate formation of dipoles at the P3HT:PCBM interfaces upon annealing. These dipoles are shown to reduce geminate recombination of separated charges at the interfaces. The good performance of the rr-P3HT:PCBM blend compared to APFO3:PCBM and many other donor-acceptor systems can thus at least partially be ascribed to the ordered nature of rr-P3HT and the formation of interfacial dipoles as a result of annealing.

Bibliography

[1] A. J. Heeger. Nobel lecture: Semiconducting and metallic polymers: The fourth generation of polymeric materials. *Rev. Mod. Phys.* **73**, 681 (2001).

[2] B. O'Regan and M. Grätzel. A low-cost, high-efficiency solar cell based on dye-sensitized colloidal TiO_2 films. *Nature* **353**, 737 (1991).

[3] G. Yu, J. Gao, J. C. Hummelen, F. Wudl, and A. J. Heeger. Polymer photovoltaic cells: Enhanced efficiencies via a network of internal donor-acceptor heterojunctions. *Science* **270**, 1789 (1995).

[4] M. Hiramoto, H. Fujiwara, and M. Yokoyama. Three-layered organic solar cell with a photoactive interlayer of codeposited pigments. *Appl. Phys. Lett.* **58**, 1062 (1991).

[5] A. Yella, H.-W. Lee, H. N. Tsao, C. Yi, A. K. Chandiran, M. Nazeeruddin, E. W.-G. Diau, C.-Y. Yeh, S. M. Zakeeruddin, and M. Grätzel. Porphyrin-sensitized solar cells with cobalt (II/III)-based redox electrolyte exceed 12 percent efficiency. *Science* **334**, 629 (2011).

[6] Heliatek. `http://www.heliatek.com/`. Accessed 28.8.2012.

[7] G. Li, R. Zhu, and Y. Yang. Polymer solar cells. *Nat. Photonics* **6**, 153 (2012).

[8] H. Hoppe and N. S. Sariciftci. Morphology of polymer/fullerene bulk heterojunction solar cells. *J. Mater. Chem.* **16**, 45 (2006).

[9] M. Jørgensen, K. Norrman, and F. C. Krebs. Stability/degradation of polymer solar cells. *Sol. Energ. Mat. Sol. C.* **92**, 686 (2008).

[10] H. T. Nicolai, M. Kuik, G. A. H. Wetzelaer, B. de Boer, C. Campbell, C. Risko, J. L. Brédas, and P. W. M. Blom. Unification of trap-limited electron transport in semiconducting polymers. *Nature Mater.* **11**, 882 (2012).

[11] A. Pivrikas, N. S. Sariciftci, G. Juška, and R. Österbacka. A review of charge transport and recombination in polymer/fullerene organic solar cells. *Prog. Photovolt: Res. Appl.* **15**, 677 (2007).

[12] W. Ma, C. Yang, X. Gong, K. Lee, and A. J. Heeger. Thermally stable, efficient polymer solar cells with nanoscale control of the interpenetrating network morphology. *Adv. Funct. Mater.* **15**, 1617 (2005).

[13] C. M. Björström Svanström, J. Rysz, A. Bernasik, A. Budkowski, F. Zhang, O. Inganäs, M. R. Andersson, K. O. Magnusson, J. J. Benson-Smith, J. Nelson, and E. Moons. Device performance of APFO-3/PCBM solar cells with controlled morphology. *Adv. Mat.* **21**, 4398 (2009).

[14] K. M. Coakley and M. D. McGehee. Conjugated polymer photovoltaic cells. *Chem. Mater.* **16**, 4533 (2004).

[15] S. Glenis, G. Horowitz, G. Tourillon, and F. Garnier. Electrochemically grown polythiophene and poly(3-methylthiophene) organic photovoltaic cells. *Thin Solid Films* **111**, 93 (1984).

[16] P. E. Shaw, A. Ruseckas, and I. D. W. Samuel. Exciton diffusion measurements in poly(3-hexylthiophene). *Adv. Mat.* **20**, 3516 (2008).

[17] N. S. Sariciftci, L. Smilowitz, A. J. Heeger, and F. Wudl. Photoinduced electron transfer from a conducting polymer to buckminsterfullerene. *Science* **258**, 1474 (1992).

[18] W. Ma, C. Yang, and A. J. Heeger. Spatial fourier-transform analysis of the morphology of bulk heterojunction materials used in "plastic" solar cells. *Adv. Mat.* **19**, 1387 (2007).

[19] Y. M. Nam, J. Huh, and W. H. Jo. Optimization of thickness and morphology of active layer for high performance of bulk-heterojunction organic solar cells. *Sol. Energ. Mat. Sol. C.* **94**, 1118 (2010).

[20] S. R. Forrest. The limits to organic photovoltaic cell efficiency. *MRS Bull.* **30**, 28 (2005).

[21] F. Zhang, K. G. Jespersen, C. Björström, M. Svensson, M. R. Andersson, V. Sundström, K. Magnusson, E. Moons, A. Yartsev, and O. Inganäs. Influence of solvent mixing on the morphology and performance of solar cells based on polyfluorene copolymer/fullerene blends. *Adv. Funct. Mater.* **16**, 667 (2006).

[22] M. Campoy-Quiles, T. Ferenczi, T. Agostinelli, P. G. Etchegoin, Y. Kim, T. D. Anthopoulos, P. N. Stavrinou, D. D. C. Bradley, and J. Nelson. Morphology evolution via self-organization and lateral and vertical diffusion in polymer:fullerene solar cell blends. *Nature Mater.* **7**, 158 (2008).

[23] L.-M. Chen, Z. Hong, G. Li, and Y. Yang. Recent progress in polymer solar cells: Manipulation of polymer:fullerene morphology and the formation of efficient inverted polymer solar cells. *Adv. Mat.* **21**, 1434 (2009).

[24] D. Chen, A. Nakahara, D. Wei, D. Nordlund, and T. P. Russell. P3HT/PCBM bulk heterojunction organic photovoltaics: Correlating efficiency and morphology. *Nano Lett.* **11**, 561 (2011).

[25] T. J. Savenije, J. E. Kroeze, X. Yang, and J. Loos. The effect of thermal treatment on the morphology and charge carrier dynamics in a polythiophene–fullerene bulk heterojunction. *Adv. Funct. Mater.* **15**, 1260 (2005).

[26] V. D. Mihailetchi, H. X. Xie, B. de Boer, L. J. A. Koster, and P. W. M. Blom. Charge transport and photocurrent generation in poly(3-hexylthiophene): Methanofullerene bulk-heterojunction solar cells. *Adv. Funct. Mater.* **16**, 699 (2006).

[27] V. D. Mihailetchi, P. W. M. Blom, J. C. Hummelen, and M. T. Rispens. Cathode dependence of the open-circuit voltage of polymer:fullerene bulk heterojunction solar cells. *J. Appl. Phys.* **94**, 6849 (2003).

[28] D. Beljonne, J. Cornil, J. L. Brédas, and R. H. Friend. Theoretical investigation of the lowest singlet and triplet excited states in oligo(phenylene vinylene)s and oligothiophenes. *Synt. Met.* **76**, 61 (1996).

[29] M. Pope and C. E. Swenberg. *Electronic Processes in Organic Crystals and Polymers*. Oxford University Press, second edition (1999).

[30] M. A. Stevens, C. Silva, D. M. Russell, and R. H. Friend. Exciton dissociation mechanisms in the polymeric semiconductors poly(9,9-dioctylfluorene) and poly(9,9-dioctylfluorene-co-benzothiadiazole). *Phys. Rev. B* **63**, 165213 (2001).

[31] Q.-H. Xu, D. Moses, and A. J. Heeger. Direct observation of a time-delayed intermediate state generated via exciton-exciton annihilation in polyfluorene. *Phys. Rev. B* **68**, 174303 (2003).

[32] I. B. Martini, A. D. Smith, and B. J. Schwartz. Exciton-exciton annihilation and the production of interchain species in conjugated polymer films: Comparing the ultrafast stimulated emission and photoluminescence dynamics of MEH-PPV. *Phys. Rev. B* **69**, 035204 (2004).

[33] A. J. Heeger, S. Kivelson, J. R. Schrieffer, and W. P. Su. Solitons in conducting polymers. *Rev. Mod. Phys.* **60**, 781 (1988).

[34] R. Österbacka, C. P. An, X. M. Jiang, and Z. V. Vardeny. Two-dimensional electronic excitations in self-assembled conjugated polymer nanocrystals. *Science* **287**, 839 (2000).

[35] D. Beljonne, J. Cornil, H. Sirringhaus, P. J. Brown, M. Shkunov, R. H. Friend, and J.-L. Brédas. Optical signature of delocalized polarons in conjugated polymers. *Adv. Funct. Mater.* **11**, 229 (2001).

[36] P. A. Lane, X. Wei, and Z. V. Vardeny. Spin and spectral signatures of polaron pairs in π-conjugated polymers. *Phys. Rev. B* **56**, 4626 (1997).

[37] E. L. Frankevich, A. A. Lymarev, I. Sokolik, F. E. Karasz, S. Blumstengel, R. H. Baughman, and H. H. Hörhold. Polaron-pair generation in poly(phenylene vinylenes). *Phys. Rev. B* **46**, 9320 (1992).

[38] M. Yan, L. J. Rothberg, F. Papadimitrakopoulos, M. E. Galvin, and T. M. Miller. Spatially indirect excitons as primary photoexcitations in conjugated polymers. *Phys. Rev. Lett.* **72**, 1104 (1994).

[39] H. A. Mizes and E. M. Conwell. Photoinduced charge transfer in poly(*p* -phenylene vinylene). *Phys. Rev. B* **50**, 11243 (1994).

[40] C. J. Brabec, G. Zerza, G. Cerullo, S. D. Silvestri, S. Luzzati, J. C. Hummelen, and S. Sariciftci. Tracing photoinduced electron transfer process in conjugated polymer/fullerene bulk heterojunctions in real time. *Chem. Phys. Lett.* **340**, 232 (2001).

[41] L. Goris, K. Haenen, M. Nesládek, P. Wagner, D. Vanderzande, L. Schepper, J. D'haen, L. Lutsen, and J. Manca. Absorption phenomena in organic thin films for solar cell applications investigated by photothermal deflection spectroscopy. *J. Mater. Sci.* **40**, 1413 (2005).

[42] L. Goris, A. Poruba, L. Hod'ákova, M. Vaněček, K. Haenen, M. Nesládek, P. Wagner, D. Vanderzande, L. De Schepper, and J. V. Manca. Observation of the subgap optical absorption in polymer-fullerene blend solar cells. *Appl. Phys. Lett.* **88**, 052113 (2006).

[43] J. J. Benson-Smith, L. Goris, K. Vandewal, K. Haenen, J. V. Manca, D. Vanderzande, D. D. C. Bradley, and J. Nelson. Formation of a ground-state charge-transfer complex in polyfluorene/[6,6]-phenyl-C61 butyric acid methyl ester (PCBM) blend films and its role in the function of polymer/PCBM solar cells. *Adv. Funct. Mater.* **17**, 451 (2007).

[44] M. Hallermann, S. Haneder, and E. D. Como. Charge-transfer states in conjugated polymer/fullerene blends: Below-gap weakly bound excitons for polymer photovoltaics. *Appl. Phys. Lett.* **93**, 053307 (2008).

[45] T. Drori, C.-X. Sheng, A. Ndobe, S. Singh, J. Holt, and Z. V. Vardeny. Below-gap excitation of pi-conjugated polymer-fullerene blends: implications for bulk organic heterojunction solar cells. *Phys. Rev. Lett.* **101**, 037401 (2008).

[46] K. Vandewal, A. Gadisa, W. D. Oosterbaan, S. Bertho, F. Banishoeib, I. Van Severen, L. Lutsen, T. J. Cleij, D. Vanderzande, and J. V. Manca. The relation between open-circuit voltage and the onset of photocurrent generation by charge-transfer absorption in polymer:fullerene bulk heterojunction solar cells. *Adv. Funct. Mater.* **18**, 2064 (2008).

[47] J. Holt, S. Singh, T. Drori, Y. Zhang, and Z. V. Vardeny. Optical probes of π-conjugated polymer blends with strong acceptor molecules. *Phys. Rev. B* **79**, 195210 (2009).

[48] M. Hallermann, I. Kriegel, E. Da Como, J. M. Berger, E. von Hauff, and J. Feldmann. Charge transfer excitons in polymer/fullerene blends: The role of morphology and polymer chain conformation. *Adv. Funct. Mater.* **19**, 3662 (2009).

[49] K. Vandewal, K. Tvingstedt, A. Gadisa, O. Inganäs, and J. V. Manca. On the origin of the open-circuit voltage of polymer-fullerene solar cells. *Nature Mater.* **8**, 904 (2009).

[50] T. Drori, J. Holt, and Z. V. Vardeny. Optical studies of the charge transfer complex in polythiophene/fullerene blends for organic photovoltaic applications. *Phys. Rev. B* **82**, 075207 (2010).

[51] K. Tvingstedt, K. Vandewal, A. Gadisa, F. Zhang, J. Manca, and O. Inganäs. Electroluminescence from charge transfer states in polymer solar cells. *J. Am. Chem. Soc.* **131**, 11819 (2009).

[52] M. A. Faist, T. Kirchartz, W. Gong, R. S. Ashraf, I. McCulloch, J. C. de Mello, N. J. Ekins-Daukes, D. D. C. Bradley, and J. Nelson. Competition between the charge transfer state and the singlet states of donor or acceptor limiting the efficiency in polymer:fullerene solar cells. *J. Am. Chem. Soc.* **134**, 685 (2012).

[53] D. Veldman, S. C. J. Meskers, and R. A. J. Janssen. The energy of charge-transfer states in electron donor-acceptor blends: Insight into the energy losses in organic solar cells. *Adv. Funct. Mater.* **19**, 1939 (2009).

[54] T. Liu and A. Troisi. Absolute rate of charge separation and recombination in a molecular model of the P3HT/PCBM interface. *J. Phys. Chem. C* **115**, 2406 (2011).

[55] G. Grancini, D. Polli, D. Fazzi, J. Cabanillas-Gonzalez, G. Cerullo, and G. Lanzani. Transient absorption imaging of P3HT:PCBM photovoltaic blend: Evidence for interfacial charge transfer state. *J. Phys. Chem. Lett.* **2**, 1099 (2011).

[56] J. Nelson. Continuous-time random-walk model of electron transport in nanocrystalline TiO_2 electrodes. *Phys. Rev. B* **59**, 15374 (1999).

[57] J. Nelson. Diffusion-limited recombination in polymer-fullerene blends and its influence on photocurrent collection. *Phys. Rev. B* **67**, 155209 (2003).

[58] R. C. I. MacKenzie, T. Kirchartz, G. F. A. Dibb, and J. Nelson. Modeling nongeminate recombination in P3HT:PCBM solar cells. *J. Phys. Chem. C* **115**, 9806 (2011).

[59] R. A. Marcus and N. Sutin. Electron transfers in chemistry and biology. *Biochim. Biophys. Acta* **811**, 265 (1985).

[60] O. Epshtein, G. Nakhmanovich, Y. Eichen, and E. Ehrenfreund. Dispersive dynamics of photoexcitations in conjugated polymers measured by photomodulation spectroscopy. *Phys. Rev. B* **63**, 125206 (2001).

[61] O. Epshtein, Y. Eichen, E. Ehrenfreund, M. Wohlgenannt, and Z. V. Vardeny. Linear and nonlinear photoexcitation dynamics in π-conjugated polymers. *Phys. Rev. Lett.* **90**, 046804 (2003).

[62] M. Westerling, C. Vijila, R. Österbacka, and H. Stubb. Dispersive and nondispersive recombination of photoexcitations in disordered organic solids. *Phys. Rev. B* **69**, 245201 (2004).

[63] S. C. J. Meskers, P. A. van Hal, A. J. H. Spiering, J. C. Hummelen, A. F. G. van der Meer, and R. A. J. Janssen. Time-resolved infrared-absorption study of photoinduced charge transfer in a polythiophene-methanofullerene composite film. *Phys. Rev. B* **61**, 9917 (2000).

[64] A. Plonka, Y. A. Berlin, and N. I. Chekunaev. Dispersive recombination in condensed phases. *Chem. Phys. Lett.* **158**, 380 (1989).

[65] M. Scheidler, B. Cleve, H. Bässler, and P. Thomas. Monte carlo simulation of bimolecular exciton annihilation in an energetically random hopping system. *Chem. Phys. Lett.* **225**, 431 (1994).

[66] S. D. Phillips, R. Worland, G. Yu, T. Hagler, R. Freedman, Y. Cao, V. Yoon, J. Chiang, W. C. Walker, and A. J. Heeger. Electroabsorption of polyacetylene. *Phys. Rev. B* **40**, 9751 (1989).

[67] J. A. Moon and J. Tauc. Interference effects in pump-probe spectroscopy of thin films. *J. Appl. Phys.* **73**, 4571 (1993).

[68] K. Lee, E. K. Miller, N. S. Sariciftci, J. C. Hummelen, F. Wudl, and A. J. Heeger. Photoinduced absorption and photoinduced reflectance in conducting polymer/methanofullerene films: Nonlinear-optical changes in the complex index of refraction. *Phys. Rev. B* **54**, 10525 (1996).

[69] M. Westerling, C. Vijila, R. Österbacka, and H. Stubb. Bimolecular recombination in regiorandom poly(3-hexylthiophene). *Chem. Phys.* **286**, 315 (2003).

[70] M. Westerling, C. Vijila, R. Österbacka, and H. Stubb. Optical studies of excited-state relaxation in poly(9,9-dihexylfluorene-co-benzothiadiazole). *Phys. Rev. B* **67**, 195201 (2003).

[71] M. Wohlgenannt, W. Graupner, G. Leising, and Z. V. Vardeny. Photogeneration and recombination processes of neutral and charged excitations in films of a ladder-type poly(*para*-phenylene). *Phys. Rev. B* **60**, 5321 (1999).

[72] M. Westerling. *Recombination Dynamics of Long-Lived Photoexcitations in π-Conjugated Polymers*. Ph.D. thesis, Åbo Akademi University (2004).

[73] G. Dellepiane, C. Cuniberti, D. Comoretto, G. F. Musso, G. Figari, A. Piaggi, and A. Borghesi. Long-lived photoexcited states in symmetrical polydicarbazolyldiacetylene. *Phys. Rev. B* **48**, 7850 (1993).

[74] R. Metzler and J. Klafter. From stretched exponential to inverse power-law: fractional dynamics, Cole-Cole relaxation processes, and beyond. *J. Non-Cryst. Solids* **305**, 81 (2002).

[75] E. Ehrenfreund, O. Epshtein, Y. Eichen, M. Wohlgenannt, and Z. V. Vardeny. Dispersive nonlinear dynamics of photoexcitations in π-conjugated polymers. *Synt. Met.* **137**, 1363 (2003).

[76] M. T. Dang, L. Hirsch, and G. Wantz. P3HT:PCBM, best seller in polymer photovoltaic research. *Adv. Mater.* **23**, 3597 (2011).

[77] R. D. McCullough, R. D. Lowe, M. Jayaraman, and D. L. Anderson. Design, synthesis, and control of conducting polymer architectures: structurally homogeneous poly(3-alkylthiophenes). *J. Org. Chem.* **58**, 904 (1993).

[78] R. D. McCullough, S. Tristram-Nagle, S. P. Williams, R. D. Lowe, and M. Jayaraman. Self-orienting head-to-tail poly(3-alkylthiophenes): new insights on structure-property relationships in conducting polymers. *J. Am. Chem. Soc.* **115**, 4910 (1993).

[79] T.-A. Chen, X. Wu, and R. D. Rieke. Regiocontrolled synthesis of poly(3-alkylthiophenes) mediated by rieke zink: Their characterization and solid-state properties. *J. Am. Chem. Soc.* **117**, 233 (1995).

[80] H. Sirringhaus, P. J. Brown, R. H. Friend, M. M. Nielsen, K. Bechgaard, B. M. W. Langeveld-Voss, A. J. H. Spiering, R. A. J. Janssen, E. W. Meijer, P. Herwig, and D. M. de Leeuw. Two-dimensional charge transport in self-organized, high-mobility conjugated polymers. *Nature* **401**, 685 (1999).

[81] R. M. Beal, A. Stavrinadis, J. H. Warner, J. M. Smith, H. E. Assender, and A. A. R. Watt. The molecular structure of polymer-fullerene composite solar cells and its influence on device performance. *Macromolecules* **43**, 2343 (2010).

[82] A. Pivrikas, G. Juška, A. J. Mozer, M. Scharber, K. Arlauskas, N. S. Sariciftci, H. Stubb, and R. Österbacka. Bimolecular recombination coefficient as a sensitive testing parameter for low-mobility solar cell materials. *Phys. Rev. Lett.* **94**, 176806 (2005).

[83] X. M. Jiang, R. Österbacka, O. Korovyanko, C. P. An, B. Horowitz, R. A. J. Janssen, and Z. V. Vardeny. Spectroscopic studies of photoexcitations in regioregular and regiorandom polythiophene films. *Adv. Funct. Mater.* **12**, 587 (2002).

[84] K. G. Jespersen, W. J. D. Beenken, Y. Zaushitsyn, A. Yartsev, M. Andersson, T. Pullerits, and V. Sundström. The electronic states of polyfluorene copolymers with alternating donor-acceptor units. *J. Chem. Phys.* **121**, 12613 (2004).

[85] O. Inganäs, M. Svensson, F. Zhang, A. Gadisa, N. K. Persson, X. Wang, and M. R. Andersson. Low bandgap alternating polyfluorene copolymers in plastic photodiodes and solar cells. *Appl. Phys. A* **79**, 31 (2004).

[86] T. Pascher. Temperature and driving force dependence of the folding rate of reduced horse heart cytochrome c. *Biochemistry* **40**, 5812 (2001).

[87] C. Rothe and A. P. Monkman. Triplet exciton migration in a conjugated polyfluorene. *Phys. Rev. B* **68**, 075208 (2003).

[88] L. Smilowitz, N. S. Sariciftci, R. Wu, C. Gettinger, A. J. Heeger, and F. Wudl. Photoexcitation spectroscopy of conducting-polymer-C_{60} composites: Photoinduced electron transfer. *Phys. Rev. B* **47**, 13835 (1993).

[89] M. C. Scharber, N. A. Schultz, N. S. Sariciftci, and C. J. Brabec. Optical- and photocurrent-detected magnetic resonance studies on conjugated polymer/fullerene composites. *Phys. Rev. B* **67**, 085202 (2003).

[90] M. Tong, C. X. Sheng, C. Yang, Z. V. Vardeny, and Y. Pang. Photoexcitation dynamics and laser action in solutions and films of PPE-PPV copolymer. *Phys. Rev. B* **69**, 155211 (2004).

[91] J. G. Müller, U. Lemmer, J. Feldmann, and U. Scherf. Precursor states for charge carrier generation in conjugated polymers probed by ultrafast spectroscopy. *Phys. Rev. Lett.* **88**, 147401 (2002).

[92] T. Virgili, D. Marinotto, C. Manzoni, G. Cerullo, and G. Lanzani. Ultrafast intrachain photoexcitation of polymeric semiconductors. *Phys. Rev. Lett.* **94**, 117402 (2005).

[93] B. Schweitzer, V. Arkhipov, U. Scherf, and H. Bässler. Geminate pair recombination in a conjugated polymer. *Chem. Phys. Lett.* **313**, 57 (1999).

[94] D. Hertel, Y. Romanovskii, B. Schweitzer, U. Scherf, and H. Bässler. The origin of the delayed emission in films of a ladder-type poly(paraphenylene). *Synt. Met.* **116**, 139 (2001).

[95] C. Cuppoletti and L. Rothberg. Persistent photoluminescence in conjugated polymers. *Synt. Met.* **139**, 867 (2003).

[96] C. Rothe and A. Monkman. Regarding the origin of the delayed fluorescence of conjugated polymers. *J. Chem. Phys.* **123**, 244904 (2005).

[97] S. De, T. Pascher, M. Maiti, K. G. Jespersen, T. Kesti, F. Zhang, O. Inganäs, A. Yartsev, and V. Sundström. Geminate charge recombination in alternating polyfluorene copolymer/fullerene blends. *J. Am. Chem. Soc.* **129**, 8466 (2007).

[98] S. De, T. Kesti, M. Maiti, F. Zhand, O. Inganäs, A. Yartsev, T. Pascher, and V. Sundström. Exciton dynamics in alternating polyfluorene/fullerene blends. *Chem. Phys.* **350**, 14 (2008).

[99] S. Braun, W. R. Salaneck, and M. Fahlman. Energy-level alignment at organic/metal and organic/organic interfaces. *Adv. Mater.* **21**, 1450 (2009).

[100] C. Tengstedt, W. Osikowicz, W. R. Salaneck, I. D. Parker, C.-H. Hsu, and M. Fahlman. Fermi-level pinning at conjugated polymer interfaces. *Appl. Phys. Lett.* **88**, 053502 (2006).

[101] M. Fahlman, A. Crispin, X. Crispin, S. K. M. Henze, M. P. de Jong, W. Osikowicz, C. Tengstedt, and W. R. Salaneck. Electronic structure of hybrid interfaces for polymer-based electronics. *J. Phys. Condens. Matter* **19**, 183202 (2007).

[102] S. Rughooputh, S. Hotta, A. J. Heeger, and F. Wudl. Chromism of soluble polythienylenes. *J. Polym. Sci., Part B: Polym. Phys.* **25**, 1071 (1987).

[103] W. R. Salaneck, O. Inganäs, B. Thémans, J. O. Nilsson, B. Sjögren, J.-E. Österholm, J. L. Brédas, and S. Svensson. Thermochromism in poly(3-hexylthiophene) in the solid state: A spectroscopic study of temperature-dependent conformational defects. *J. Chem. Phys.* **89**, 4613 (1988).

[104] P. Sehati, S. Braun, L. Lindell, X. Liu, L. M. Andersson, and M. Fahlman. Energy-level alignment at metal-organic and organic-organic interfaces in bulk-heterojunction solar cells. *IEEE J. Sel. Topics Quantum Electron.* **16**, 1718 (2010).

[105] V. I. Arkhipov, P. Heremans, and H. Bässler. Why is exciton dissociation so efficient at the interface between a conjugated polymer and an electron acceptor? *Appl. Phys. Lett.* **82**, 4605 (2003).

[106] S. Verlaak, D. Beljonne, D. Cheyns, C. Rolin, M. Linares, F. Castet, J. Cornil, and P. Heremans. Electronic structure and geminate pair energetics at organic-organic interfaces: The case of pentacene/C60 heterojunctions. *Adv. Funct. Mater.* **19**, 3809 (2009).

Svensk resumé

Målet med detta arbete har varit att klargöra fotofysiken i två solcellspolymerer, APFO3 och P3HT. APFO3 är en polymer med inbyggd donor-acceptor karaktär, som har visat lovande resultat som elektrondonerande material i organiska solceller. P3HT är det mest studerade modellmaterialet för samma ändamål. Båda används typiskt blandat med elektronacceptorn PCBM. Fotoinducerad absorption (PA) har använts på flera olika sätt för att klargöra fotoexcitationsdynamiken i dessa material. Fasinformation har använts för att urskilja excitationer med olika livstider i PA spektra, samt för att bestämma excitationernas livstider. Livstider har också bestämts genom att mäta modulationsfrekvensberoende på PA signalen, samt genom transienta PA mätningar. En modell för fotoexcitationsdynamiken i APFO3:PCBM från femtosekunder till mikrosekunder har skapats utgående från omfattande transient-PA mätningar samt mätning av fördröjd luminescens. Modellen beskriver samspelet av singlettexcitoner och vad som föreslås vara olika typer av polaronpar. Slutligen har fotofysiken vid gränsytorna i P3HT:PCBM samt dess inverkan på laddningsgenerationen och rekombinationen studerats. För detta har resultat från UV fotoelektronspektroskopi kombinerats med PA mätningar. I dessa PA mätningar har excitationsenergier både lägre och högre än det optiska gapet för P3HT använts. Resultaten visar att dipoler skapas vid gränsytorna som följd av värmebehandling av P3HT:PCBM bladningen. Dessa dipoler hämmar rekombination av laddningar som separerats vid gränsytan, och förklarar delvis den relativt höga effektiviteten för solceller baserade på P3HT:PCBM.

ISBN 978-952-12-2803-2